ERRATUM PUBLISHED 25 SEPTEMBER 2026; SEE LAST PAGE

Check for updates

CANCER

Systemically inducing trained immunity overcomes solid tumors' immunosuppressive microenvironment

Bram Priem[1,2,3]†, Lisa Willemsen[4]†, Tom Anbergen[1,3], Yuri van Elsas[1,3], Jeroen Deckers[1,3], David P. Schrijver[5], Stijn R.J. Hofstraat[5], Iris V. Messing[1], Jazz Munitz[3], Dionne Honing[1], Geoffrey Prévot[3], Yohana C. Toner[1], Judit Morla[3], William Wang[3], Anna Ranzenigo[3], Isabella Sirchia[3], Tomas Post[3,6], Raphaël Duivenvoorden[3,6], Ewelina Kluza[5], Glenn A.O. Cremers[7], Joost H.C.M Kreijtz[7], Carlos Pérez-Medina[3,8], Mandy M.T. van Leent[3,9], Abraham J.P. Teunissen[3], Roy van der Meel[5], Yi Zhou[10], Chris Glass[10], Jordi Ochando[11], Leo A.B. Joosten[12,13], Zahi A. Fayad[3], Romana T. Netea-Maier[1], Mihai G. Netea[1,14,15], Menno P.J. de Winther[4], Thijs J. Beldman[1], Arjan W. Griffioen[2], Willem J.M. Mulder[1,5]*

Copyright © 2026 The Authors, some rights reserved; exclusive licensee American Association for the Advancement of Science. No claim to original U.S. Government Works. Distributed under a Creative Commons Attribution NonCommercial License 4.0 (CC BY-NC).

Hematopoietic bone marrow progenitors are increasingly implicated as an origin of immunosuppression in cancer. We have previously shown that trained immunity induction using nanomedicine potentiates checkpoint blockade therapy. Here, we studied how this approach's induction of trained immunity systemically overcomes the immunosuppressive tumor microenvironment. We found changes in the tumor microenvironment to mirror functional changes in the hematopoietic system in a melanoma mouse model. Single cell sequencing methods disclosed a shift in the tumor-associated macrophage population from immunosuppressive to antitumorigenic. Uniquely, a trained immunity and checkpoint blockade combination therapy mobilized natural killer cells which, in conjunction with the functional changes in the myeloid cell compartment, effectively activated T cells. Last, we established the effectiveness of our approach in mouse models of breast, lung, and pancreatic cancer. Collectively, our data show that the systemic induction of trained immunity rebalances the immune system for effective checkpoint blockade therapy.

INTRODUCTION

Accumulating evidence implicates bone marrow progenitor cells in cancer-induced immunosuppression. Preclinical and clinical studies suggest that—through the release of cytokines, chemokines, and metabolites—tumors can induce systemic immunosuppression already from the level of bone marrow hematopoietic stem and progenitor cells (*1*, *2*). The resulting progenitor cells' tolerogenic state drives the formation of immune cells with an aberrant functional program and their accumulation in the tumor microenvironment. In line with this concept, Rabold *et al.* (*3*) showed that myeloid cells of patients with thyroid cancer display functional changes before infiltrating the tumor, with the bone marrow playing a pivotal role in immunosuppression.

Trained immunity, a concept originally studied in the context of infectious diseases, refers to myeloid cells' hyperresponsive state after encountering specific stimuli that engage pattern-recognizing receptors, including Dectin-1 and nucleotide-binding oligomerization domain-containing protein 2 (NOD2) (*4*–*6*). The longevity of the trained immunity program in peripheral immune cells is ensured by epigenetic modifications in bone marrow progenitor cells, leading to a heightened and more effective innate immune response upon subsequent exposures to heterologous stimuli (*7*). As trained immunity can be considered the immunologically opposite state of immunosuppression, its systemic induction may be a compelling strategy to overcome the immunosuppressive tumor microenvironment (*8*).

Nanobiologics are lipid nanoparticles that integrate apolipoprotein A1 and can be functionalized with lipophilic and amphiphilic drug conjugates, such as muramyl tripeptide phosphatidylethanolamine (MTP-PE), which activates NOD2. We have previously shown that pharmacologically inducing trained immunity with bone marrow–avid and muramyl tripeptide–functionalized nanobiologics (MTP-HDL) indeed overcomes systemic immunosuppression and ameliorates checkpoint inhibitor (CI) therapy against cancer in the refractory B16F10 mouse melanoma model (*9*).

In pursuit of understanding how systemically inducing trained immunity with MTP-HDL reshapes the tumor microenvironment, here, we use single-cell sequencing techniques and immune landscape profiling. In addition to examining functional changes in monocytes, we study natural killer (NK) cells' role in antitumor effects and the impact of inducing trained immunity on T cell activation. As we hypothesize that inducing trained immunity may have

[1]Department of Internal Medicine, Radboud University Medical Center, Nijmegen, Netherlands. [2]Angiogenesis Laboratory, Amsterdam UMC, Cancer Center Amsterdam, Amsterdam, Netherlands. [3]Biomedical Engineering and Imaging Institute, Icahn School of Medicine at Mount Sinai, New York, NY, USA. [4]Department of Medical Biochemistry, Amsterdam Cardiovascular Sciences, Atherosclerosis & Ischemic Syndromes; Amsterdam Institute for Infection and Immunity, Inflammatory diseases, (AI&II), Amsterdam University Medical Centers, location University of Amsterdam, Amsterdam, Netherlands. [5]Laboratory of Chemical Biology, Department of Biochemical Engineering, Eindhoven University of Technology, Eindhoven, Netherlands. [6]Department of Nephrology, Radboud Institute for Molecular Life Sciences, Radboud University Medical Center, Nijmegen, Netherlands. [7]Trained Therapeutix Discovery, 5349 AB Oss, Netherlands. [8]Centro Nacional de Investigaciones Cardiovasculares Carlos III, Madrid, Spain. [9]Cardiovascular Research Institute, Icahn School of Medicine at Mount Sinai, New York, NY, USA. [10]Department of Cellular and Molecular Medicine, School of Medicine, University of California, San Diego, La Jolla, CA, USA. [11]Department of Medicine, Division of Hematology and Medical Oncology, Icahn School of Medicine, Tisch Cancer Institute at Mount Sinai, New York, NY, USA. [12]Department of Internal Medicine and Radboud Institute of Molecular Life Sciences (RIMLS), Radboud University Medical Center, Nijmegen, Netherlands. [13]Department of Medical Genetics, Iuliu Haţieganu University of Medicine and Pharmacy, Cluj-Napoca, Romania. [14]Human Genomics Laboratory, Craiova University of Medicine and Pharmacy, Craiova, Romania. [15]Department for Immunology & Metabolism, Life and Medical Sciences Institute (LIMES), University of Bonn, Bonn, Germany.
*Corresponding author. Email: willem.mulder@radboudumc.nl
†These authors contributed equally to this work.

Downloaded from https://www.science.org at Technische University Eindhoven on October 30, 2026

ERRATUM PUBLISHED 25 SEPTEMBER 2026; SEE LAST PAGE

benefits in a wide range of solid cancers that are characterized by myeloid cell–induced immunosuppression, we applied MTP-HDL–enhanced immunotherapy in checkpoint inhibition blockade refractory mouse models of lung, breast, and pancreatic cancer.

RESULTS

MTP-HDL treatment induces a metabolic shift in myeloid cells

We previously demonstrated the antitumor efficacy of our nanobiologic MTP-HDL therapy, as a single agent and in combination with CIs, in an experimental melanoma model (Fig. 1A). To disentangle the molecular mechanisms of these effects, we conducted an in vivo experiment in C57BL/6 mice that were subcutaneously inoculated with 1×10^5 B16F10 melanoma cells. One week after inoculation, when tumors became palpable, mice were subjected to one of four treatments: (i) control regimen with phosphate-buffered saline (PBS), (ii) intravenous monotherapy with MTP-HDL (1.5 mg/kg), (iii) combined intraperitoneal anti–PD-1 and anti–CTLA-4 CI therapy each at 200 μg, or (iv) a regimen involving MTP-HDL treatment in conjunction with anti–PD-1 and anti–CTLA-4 combination therapy (MTP-HDL + CI) (Fig. 1B). In line with our previous findings (*9*), the anti–PD-1 and anti–CTLA-4 combination therapy did not significantly inhibit tumor growth (PBS: 262 ± 141 mm^3, CI: 215 ± 129 mm^3; $P = 0.7462$). Conversely, MTP-HDL + CI treatment manifested a substantial suppression of tumor growth compared to PBS and both monotherapy groups. (MTP-HDL: 152 ± 111 mm^3, MTP-HDL + CI: 40 ± 32 mm^3; PBS versus MTP-HDL + CI: $P = 0.0004$; CI versus MTP-HDL + CI: $P = 0.0002$; MTP-HDL versus MTP-HDL + CI: $P = 0.0121$) (Fig. 1C).

Trained immunity induction by MTP-HDL treatment and its effect on myeloid cells from spleen and bone marrow are, at least in part, responsible for the observed antitumor effects (*9*). One of the trained immunity hallmarks is a metabolic shift in myeloid cells, mainly through enhanced glycolytic activity (*10*). To qualitatively evaluate enhanced glycolytic activity following MTP-HDL treatment, we studied ^{18}F-fluorodeoxyglucose (^{18}F-FDG) uptake in the bone marrow using in vivo position emission tomography with computed tomography (PET-CT) imaging (Fig. 1D). After euthanizing the animals, we performed fully quantitative ex vivo gamma counting of ^{18}F-FDG uptake. In the bone marrow and spleen tissues, we measured significantly increased ^{18}F-FDG uptake in the two groups that incorporated MTP-HDL treatment (PBS versus MTP-HDL: $P = 0.0307$; PBS versus MTP-HDL + CI: $P = 0.0032$) (Fig. 1E).

While measuring ^{18}F-FDG uptake allows the quantitative assessment of the metabolic activity at the organ level, it is not suitable for discriminating between increased activity of individual cells and a higher cell burden (Fig. 1F and fig. S1, A to C). Therefore, we performed flow cytometry analyses on bone marrow, spleen, and tumor tissues using an antibody staining for the Glucose transporter 1 (GLUT-1; Fig. 1G). Enhanced GLUT-1 expression on membranes is associated with augmented glycolytic and metabolic activity of cells (*11*). We found GLUT-1 expression in myeloid cells of the spleen and bone marrow to be significantly up-regulated in the groups receiving MTP-HDL treatment (Fig. 1H). In the bone marrow, we found more pronounced GLUT-1 up-regulation in neutrophils (PBS versus MTP-HDL: $P = 0.0028$; PBS versus MTP-HDL + CI: $P = 0.0269$) relative to the monocytes (PBS versus MTP-HDL: $P < 0.0001$; PBS versus MTP-HDL + CI: $P = 0.0836$). Relative to what we observed in the bone marrow, GLUT-1 overexpression in the spleen was more prominent for both neutrophils (PBS versus MTP-HDL: $P = 0.0499$; PBS versus MTP-HDL + CI: $P = 0.0007$) and monocytes (PBS versus MTP-HDL: $P = 0.0004$; PBS versus MTP-HDL + CI: $P = 0.0006$).

The higher cellular glucose requirement is facilitated by increased GLUT-1 expression and is associated with augmented glycolysis (*11*). In isolated splenocytes and bone marrow cells from mice treated with either PBS or MTP-HDL, we used CENCAT (cellular energetics through noncanonical amino acid tagging) to investigate glycolysis rates of monocytes and neutrophils using flow cytometry (*12*). CENCAT flow cytometry uncovered that bone marrow monocytes underwent a metabolic shift from oxidative phosphorylation to glycolysis ($P = 0.0007$). In the spleen, neutrophils experienced a similar metabolic shift ($P = 0.0201$; Fig. 1I). Histologically, we did not measure discernible differences in the amount and spatial distribution of immune cells among different populations within the tumor microenvironment (Fig. 2, A and B, and fig. S1D). Strikingly, in the tumor microenvironment, we also observed that MTP-HDL in combination with checkpoint inhibition blockade resulted in a significant up-regulation of GLUT-1 in both monocytes (PBS versus MTP-HDL: $P = 0.0984$; PBS versus MTP-HDL + CI: $P = 0.0058$) and neutrophils (PBS versus MTP-HDL: $P = 0.1791$; PBS versus MTP-HDL + CI: $P = 0.0400$) (Fig. 2C). As we hypothesize that the observed metabolic changes in tumor myeloid cells are due to infiltrating monocytes, we set out to functionally profile the tumor microenvironment. Collectively, the data demonstrate that systems-wide functional changes of immune cells, rather than shifts in cell populations within the tumor microenvironment, are responsible for the observed antitumor effects.

Functional changes of immune cells shape the tumor microenvironment

To gain a comprehensive understanding of trained immunity-associated functional changes in immune cells, we performed single-cell RNA sequencing (scRNA-seq) on tumor-infiltrating leukocytes from B16F10 tumors across the four treatment groups ($n = 2$, n represents the pooled tumor-infiltrating leukocytes of five mice): PBS, MTP-HDL, CI, and MTP-HDL + CI, all administered at previously specified dosages (Fig. 2D). Following B16F10 tumor inoculation in C57BL/6 mice, we initiated treatments on day 0. One day after the final MTP-HDL injection, tumors were excised from euthanized mice, digested, and subsequently sorted. The scRNA-seq analysis of sorted CD45$^+$ tumor-infiltrating cells yielded data for a total of 33×10^3 cells (Fig. 2E and fig. S2A).

We subsequently identified different subpopulations in the tumor-infiltrating immune cells by computationally pooling data from the four treatment groups and applying graph-based clustering. Through the assessment of well-established cell type markers, we defined 13 distinct clusters. Six of which were specific to lymphocytes, whereas six pertained to myeloid lineages, including neutrophils, conventional dendritic cells (cDCs), and plasmacytoid DCs. In addition, we recognized a cluster expressing marker genes from multiple populations (Fig. 2, F and G, and fig. S2, B and C). Broadly, the different populations can be categorized into three overarching groups: myeloid cells, B cells, and other lymphoid cells. These populations, characterized through scRNA-seq, display no discernible shift in cell counts across different treatment groups, a conclusion we further substantiated by flow cytometry analysis (fig. S3, A and B).

Downloaded from https://www.science.org at Technische University Eindhoven on October 30, 2026

ERRATUM PUBLISHED 25 SEPTEMBER 2026; SEE LAST PAGE

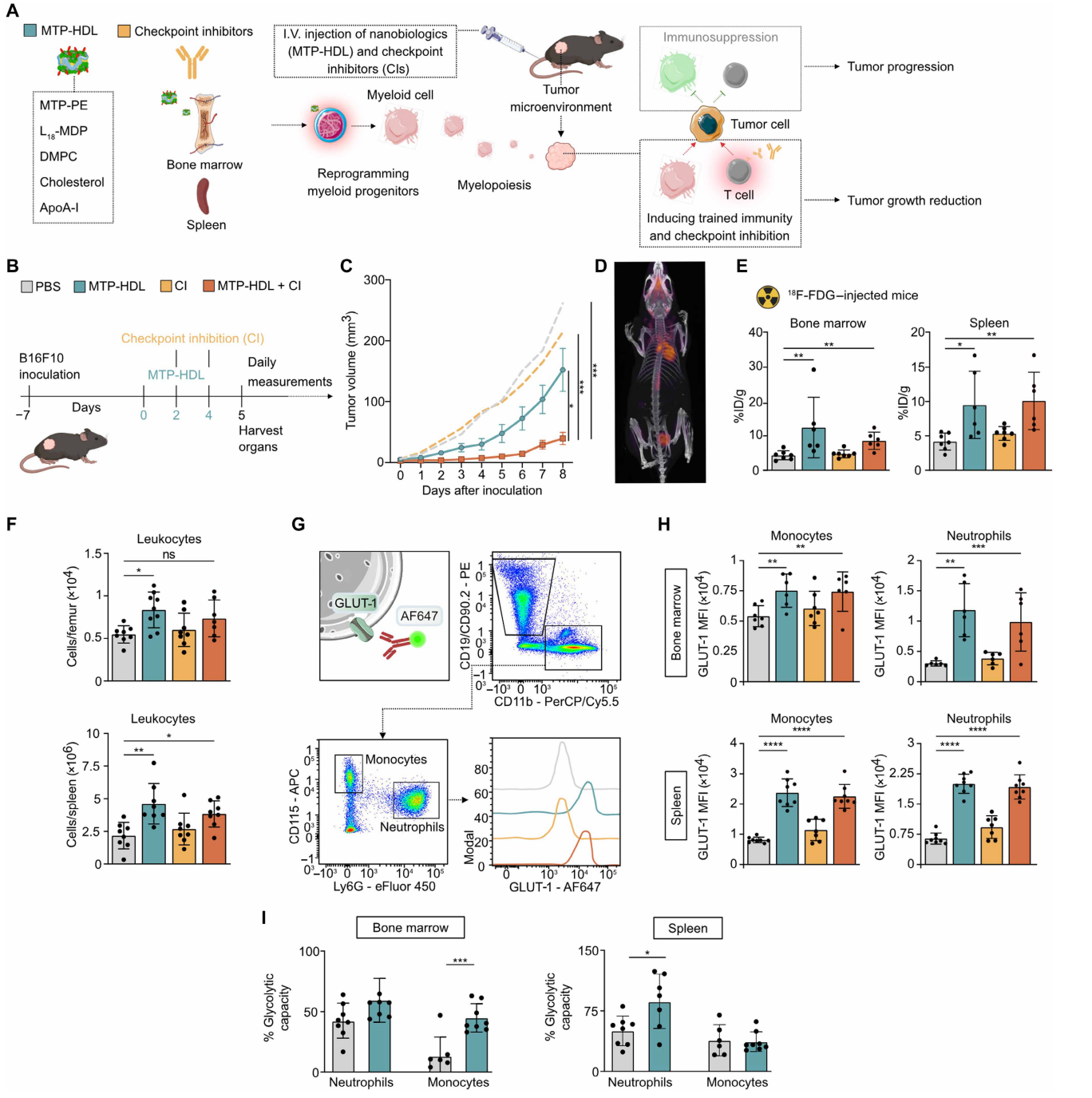

Fig. 1. MTP-HDL treatment induces a metabolic shift in myeloid cells. (**A**) Overview of preceding study (*9*) in which we developed a bone marrow-avid and trained immunity inducing nanoparticle named MTP-HDL. Through extensive analysis of the bone marrow, we highlighted the various effects this particle elicits on myeloid progenitors in the bone marrow. We finalized the study by showing that MTP-HDL is an effective monotherapy to treat B16F10 melanoma in a C57BL/6 mouse model, and it potentiates CI therapy in this otherwise refractory model. (**B**) Schematic overview of treatment regimen. Mice were treated with either PBS, three injections of MTP-HDL (1.5 mg/kg), anti–CTLA-4 and anti–PD-1 at 200 μg each, or combination therapy of MTP-HDL and CIs. (**C**) Tumor growth in B16F10 inoculated C57BL/6 mice. Results show significant decrease in tumor growth of combination therapy compared to all other groups ($n = 9/10$ per group). (**D**) Qualitative FDG PET-CT image of a C57BL/6 mouse. (**E**) Gamma counting of the bone marrow/spleen posttreatment shows significant higher uptake in groups containing MTP-HDL ($n = 6$ to 7 per group). (**F**) Flow cytometry showing total number of cells per femur/spleen posttreatment ($n = 7$ to 9 per group). (**G**) Flow plots showing gating strategy to get GLUT-1 expression of monocytes and neutrophils. (**H**) GLUT-1 expression of bone marrow/spleen monocytes and neutrophils displays significantly higher expression of GLUT-1 in groups containing MTP-HDL ($n = 6$ to 8 per group). (**I**) Glycolytic capacity as measured by CENCAT flow cytometry of neutrophils and monocytes in bone marrow and spleen ($n = 6$ to 8 per group). For all panels, data are presented as means ± SD and means ± SEM for tumor growth experiments. For the tumor growth experiment, significance shown in the graph is that of the tumor growth rate. *$P < 0.05$, **$P < 0.01$, ***$P < 0.001$, and ****$P < 0.0001$. ns, not significant. APC, allophycocyanin; PE, phycoerythrin; %ID/g, percentage injected dose per gram (%ID/g); MFI, mean fluorescence intensity.

Downloaded from https://www.science.org at Technische University Eindhoven on October 30, 2026

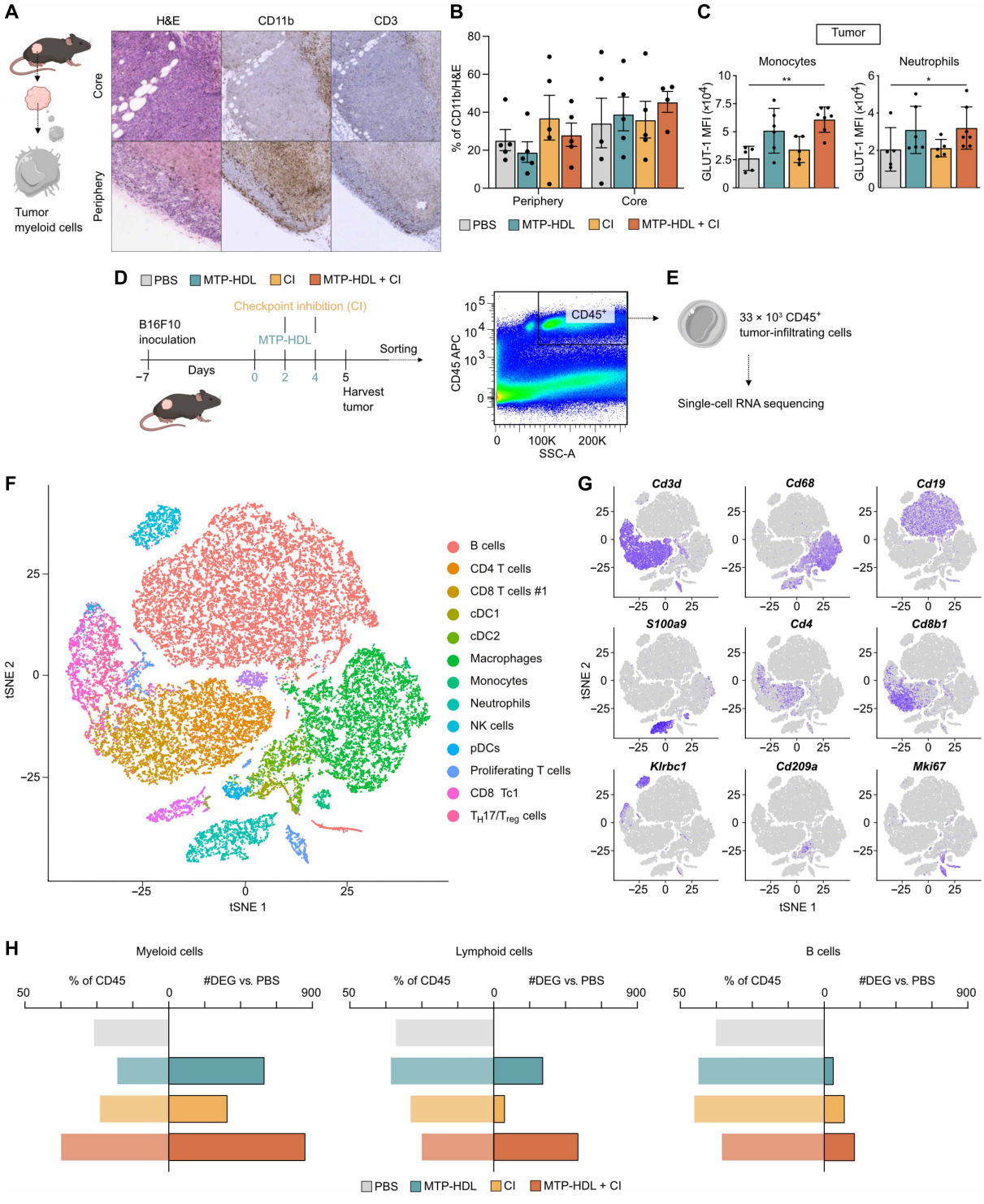

Fig. 2. Transcriptional changes of immune cells shape the tumor microenvironment. (**A**) Qualitative histology images of the tumor [hematoxylin and eosin (H&E), CD1bb staining, and CD3 staining], tumors excised day after last treatment with MTP-HDL. (**B**) Percentage of CD11b-positive cells in the core and the periphery shows no significant differences between tumor groups and a significant variation in different tumors ($n = 5$ per group). (**C**) GLUT-1 expression of tumor monocytes and neutrophils displays significantly higher expression of GLUT-1 in groups containing MTP-HDL ($n = 5$ to 7 per group). (**D**) Experimental overview of the scRNA-seq setup. (**E**) In total, 33×10^3 cells were used for analysis; each treatment group was $n = 2$, and each n consisted of the tumor-infiltrating leukocytes of five mice. (**F**) tSNE plot of all analyzed cells with cluster names. (**G**) Feature plots showing main cluster markers. (**H**) Plots displaying the population shift and the differentially expressed genes (DEGs) in either myeloid cells, lymphoid cells minus B cells, or B cells. Most of the DEGs [false discovery rate (FDR) < 0.05 and fold change (FC): 0.25 > FC < −0.25] as compared to PBS are present in the lymphoid cells minus B cells and myeloid group. SSC-A, side scatter area; pDC, plasmacytoid dendritic cell; cDC, conventional DC; NK, natural killer.

Downloaded from https://www.science.org at Technische University Eindhoven on October 30, 2026

However, we did find a substantial shift in the expression profile of these populations posttreatment as compared to PBS, indicated by the number of differentially expressed genes (DEGs), defined as an adjusted *P* value below 0.05 and a fold change below −0.25 or above 0.25 (Fig. 2H). These changes were primarily observed within the myeloid and lymphoid populations and signify a functional transition of the cells present in the tumor microenvironment. It is important to understand that these methodologies merely provide a static snapshot of a fundamentally dynamic system. Predominantly, the expanding tumor microenvironment relies on a continuous fresh influx of immune cells (*13*, *14*). Therefore, the data suggest that the incumbent cells within the tumor microenvironment may not be altered, but rather newly recruited tumor-infiltrating leukocytes display this different functional profile. This is in line with the observation that transcriptional variation was identified in both treatment groups containing MTP-HDL.

A pro-inflammatory shift in myeloid cells

Several myeloid cell populations in the dataset display significant changes in gene expression for the different treatments (Fig. 3, A and B). MTP-HDL treatment caused an up-regulation of pro-inflammatory genes in neutrophils, including *S100a6*, *Ccl2*, *Pglyrp1*, *Lyz2*, *Ifitm1*, *Ifitm3*, and *Tnfaip3*. The concurrent up-regulation of genes associated with trained immunity hallmarks, including glycolysis (*Gpi1*, *Gpx1*, and *Cyba*), epigenetic remodeling (*Hist1h1c*, *Hist1h2bc*, and *Hmgb2*), and antimicrobial response (*Lyz2*, *Slpi*, *Chil1*, and *Pglyrp1*), suggests that neutrophils adopted a pro-inflammatory phenotype. We did not observe these genes' up-regulation in mice that received CI monotherapy (Fig. 3C and fig. S3C).

Tumor-associated macrophages drive immunosuppression in the tumor microenvironment. Within the macrophage cluster, we identified a high number of DEGs in all treatment groups as compared to PBS, both up-regulated (533 genes in total) and down-regulated (444 genes in total). Particularly in treatment groups involving MTP-HDL, we observed a notable change of the transcriptional program (as a single agent: 272 up and 327 down, and in combination with checkpoint inhibition: 264 up and 298 down), with a notable overlap of DEGs in both groups (179 up and 209 down) (Fig. 3D).

In addition to classical macrophage markers, the macrophage cluster we identified is characterized by the up-regulation of distinct anti-inflammatory genes. Increased *Arg1*, *Mrc1*, *Il10ra*, and *Apoe* suggest this cluster's polarization toward an immunosuppressive phenotype (*15*). Following MTP-HDL treatment, we observed profound changes in the transcriptome of macrophages present in the tumor microenvironment and determined their inflammatory status by examining individual genes. We found the down-regulation of most of these well-established anti-inflammatory markers and additionally the proangiogenic marker *Vegfa* in all treatment groups. We additionally observed that members of the *cathepsin* family (b, d, l, and s) and the *C1q* family, which are conventionally viewed as markers of a poor cancer prognosis, were down-regulated post MTP-HDL treatment (Fig. 3E) (*16*, *17*). Simultaneously, the pro-inflammatory calprotectin complex (*S100a8* and *S100a9*) was significantly up-regulated after combination treatment with MTP-HDL and checkpoint inhibition as compared to PBS (*18*). Furthermore, *Bhlhe40*, a hallmark pro-inflammatory marker intricately linked to trained immunity, was up-regulated in both single-agent MTP-HDL and combination MTP-HDL + CI treatments. This was accompanied by the up-regulation of several glycolysis genes such as *Taldo1*, *Aldao*, and *Pkm* (Fig. 3F) (*19*). These data indicate that as a result of trained immunity induction, the tumor microenvironment is enriched with macrophages exhibiting an immune active state and that this is largely achieved by a significant down-regulation of their immunosuppressive programs.

Dynamics within the macrophage cluster, which can be observed in the change of spatial arrangement in the tSNE plots between the different treatment groups, indicate that different types of macrophages are present in the tumor microenvironment (fig. S4A). To identify these subsets, unbiased clustering revealed four macrophage phenotypes (Mac 1 to Mac 4) (Fig. 3G and fig. S4B). Notably, subset MAC1 was mainly present after treatment with PBS and our combination therapy, while subsets MAC3 and MAC4 were predominantly observed after treatment with MTP-HDL (Fig. 3H). Drawing on the work of Qian *et al.* (*20*), in which the heterogeneity among macrophages within the tumoral milieu was defined into seven distinct functional groups, we identified in our comparative analysis that the MAC1 cluster showed characteristics of multiple these functional groups such as angiogenesis, inflammatory, and regulation (fig. S4C).

The closer analysis of the MAC1 cluster uncovered high expression of the described anti-inflammatory genes (Fig. 3I and fig. S4D), corroborating this cluster's immunosuppressive nature. Following MTP-HDL (combination) treatment, we found a pronounced glycolysis transcriptome signature, including up-regulation of *Slc2a1* (*Glut1*), indicative of trained immunity induction. We also observed a significant down-regulation of immunosuppressive genes, such as *ApoE*, *Trem2*, *Dab2*, *Hif1a*, and the *cathepsin* family (b, d, l, and s), which coincided with the up-regulation of pro-inflammatory genes *Itga4*, *S100a8*, and *Ace*. Besides immunosuppressive genes' broad down-regulation, the combination therapy group also displayed increased glycolysis with up-regulation of *Gadph*, *Aldoa*, *Pgk1*, and *Hk3* (*10*). These data suggest that this multifunctional cluster's shift toward a more pro-inflammatory and glycolytic profile indicates a trained phenotype.

The MAC3 and MAC4 subsets principally contained nonclassical tumor-infiltrating monocytes (Fig. 3H and fig. S4E), and both clusters mainly surface after MTP-HDL treatment. In the MAC3 cluster, we observed down-regulated anti-inflammatory genes, including *C1q* family, *Mrc1*, *Arg1*, *Vegfa*, *Mif*, and *Dab2*, while we found significant up-regulation of *Ace* in the MAC4 cluster. The MAC4 cluster also displayed significant down-regulation of the monocyte markers *Ccr2*, *Ccl2*, and *Ly6c2c*, suggesting that these cells are in the process of differentiating from monocyte to macrophage (fig. S4E) (*21*).

We hypothesize that shifts in the tumor microenvironment are due to trained immunity induction and the ensuing infiltration of immunologically active myeloid cells. These "trained" myeloid cells originate from the bone marrow and spleen. Therefore, we investigated whether the transcriptional changes in the tumor microenvironment were also present in splenic myeloid cells using a flow cytometric analysis. In macrophages residing in the spleen, we observed a significant down-regulation of the anti-inflammatory marker CD206 following treatments with MTP-HDL (PBS versus MTP-HDL: $P = 0.0008$; PBS versus MTP-HDL + CI: $P = 0.0002$). The pro-inflammatory marker inducible nitric oxide synthase (iNOS) was only up-regulated in the combination treatment group (PBS versus MTP-HDL + CI: $P = 0.0058$) (Fig. 3J). These data mirror our sequencing data from tumor-resident macrophages, jointly indicating

Downloaded from https://www.science.org at Technische University Eindhoven on October 30, 2026

ERRATUM PUBLISHED 25 SEPTEMBER 2026; SEE LAST PAGE

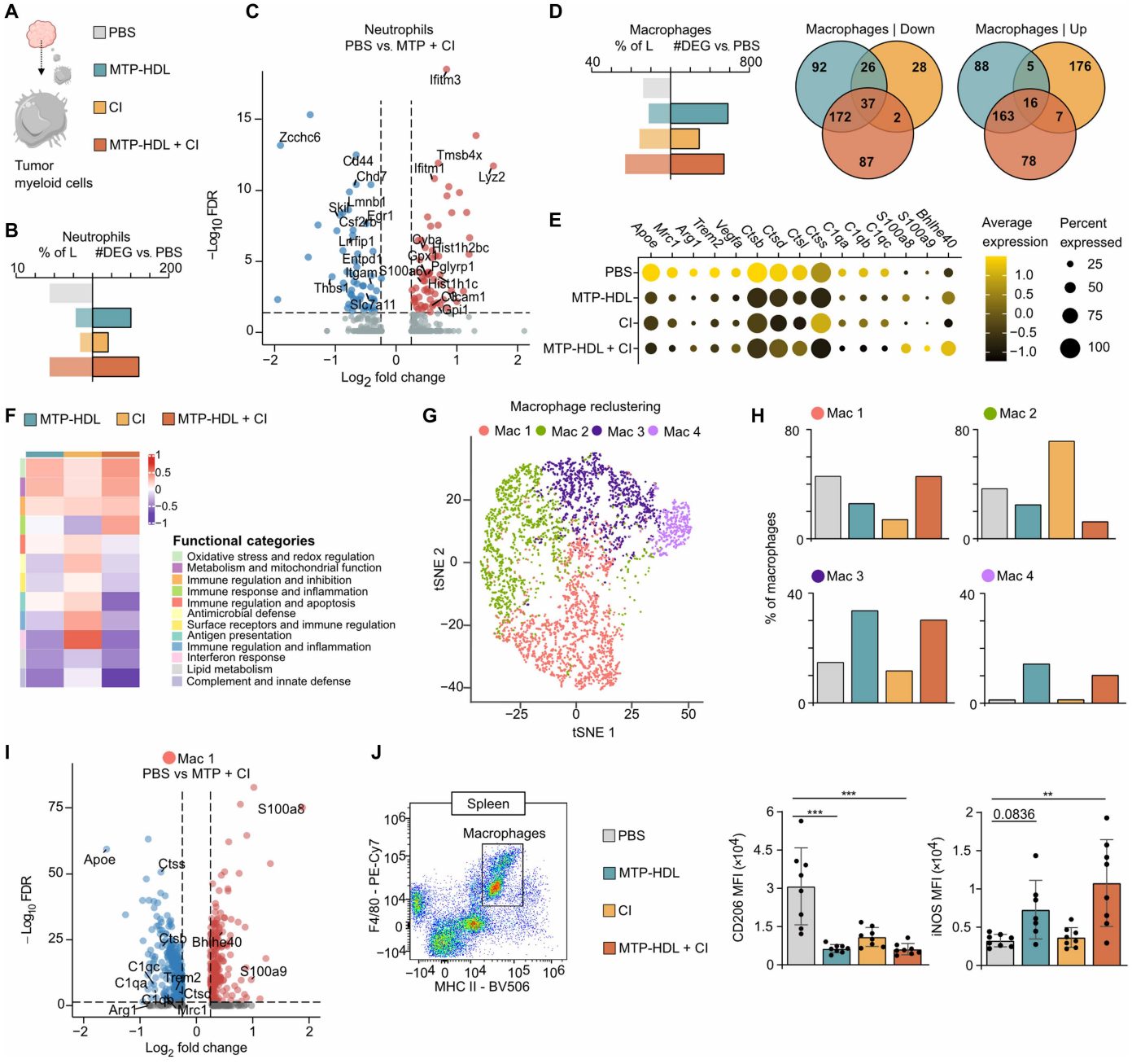

Fig. 3. A pro-inflammatory shift in tumor-associated macrophages. (**A**) This figure is mainly focused on myeloid cells as presented accompanied by a legend of the treatment groups. (**B**) Plot displaying the amount of neutrophils as a percentage of total leukocytes and the DEGs in this cluster as compared to PBS (FDR < 0.05 and fold change: 0.25 > FC < −0.25). (**C**) Volcano plot displaying up- and down-regulated genes of the neutrophil cluster when comparing PBS versus MTP + CI. (**D**) Plot displaying the amount of neutrophils as a percentage of total leukocytes and the DEGs in this cluster as compared to PBS, and Venn diagrams of up and down DEGs in all treatment arms compared to PBS (FDR < 0.05 and fold change: 0.25 > FC < −0.25). (**E**) Dot plot highlighting key pro- and anti-inflammatory genes in all treatment groups. (**F**) Heatmap displaying functional grouping of the DEGs in the macrophage cluster across all treatment groups. (**G**) tSNE plots displaying the bulk reclustering of the macrophage population identified by our original analysis. The main macrophage cluster is now divided into four subclusters Mac 1 to Mac 4. (**H**) Bar graphs displaying the distribution of macrophages in the different clusters between different treatment groups. (**I**) Volcano plot displaying up- and down-regulated genes of the Mac 1 cluster when comparing PBS versus MTP + CI. (**J**) Flow cytometry analysis of CD206 and inducible nitric oxide synthase (iNOS) in splenic macrophages. MFI of CD206 is significantly lower in all treatment groups as compared to PBS. iNOS is only significantly up-regulated in the combination therapy group ($n = 8$ per group). All genes mentioned are significant, defined as an adjusted P value below 0.05 and a fold change below −0.25 or above 0.25. For all panels, data are presented as means ± SD. $^{**}P < 0.01$ and $^{***}P < 0.001$. ns, not significant, or significance is given.

Downloaded from https://www.science.org at Technische University Eindhoven on October 30, 2026

that while MTP-HDL is sufficient to inhibit immunosuppressive signatures, the addition of checkpoint inhibition enhances the ability of macrophages to become more immunologically active. This phenomenon aligns with the characteristics of checkpoint inhibition that Gubin *et al.* (*22*) have described.

NK cells are activated following MTP-HDL treatment

Several clusters in our immune landscape tumor profiling analyses encompassed transcriptomic characteristics of multiple cell types, which was most pronounced for lymphoid cell clusters. To further characterize these different populations, we reclustered the lymphoid populations, excluding B cells (Fig. 4A). This resulted in nine distinct lymphoid populations, as compared to the previous five, effectively separating T helper 17 (T_H17) and regulatory T (T_{reg}) cells in two different clusters (Fig. 4A and fig. S5, A and B).

The different treatment affected three distinct T cell clusters, identified as CD4, CD8, and CD8 effector cells, with the combination therapy having the largest impact (Fig. 4B). All three T cell clusters displayed increased ribosomal activity, with higher expression of ribosomal genes (*Rpl* and *Rps*) and translation factors such as *Eif3h*. Combination therapy also resulted in higher expression of *Socs1*, *Batf*, and *Socs3,* indicating activation-coupled negative feedback. However, the lack of canonical expression markers such as *Pdcd1*, *Lag3*, or *Ctla4* indicate preserved T cell effector capacity. Both CI monotherapy and the combination therapy with MTP-HDL showed modest up-regulation of interferon-stimulated genes (*Stat1*, *Igtp*, and *Tap1*) (Fig. 4C).

One of the populations we did not previously detect in our analyses, are the "rapid response" (RR) T cells which consist of pro-inflammatory T cells with high expression of the interferon-related genes *Ifit1*, *Ifit3*, and *Irf7*. Unexpectedly, several of the highest expressed genes in these cells were quiescent markers *Slfn1* and *Slfn5*, suggesting that this cell population is simultaneously pro-inflammatory and dormant (*23*). Notably, following treatments containing MTP-HDL, this population appeared to vanish in the analysis. Taking the previously stated plasticity of the tumor microenvironment into account, our data suggest that these cells either do not accumulate in the tumor or do so in a different, more active form, possibly by shedding quiescent markers. The existence of these highly pro-inflammatory, dormant T cells that can act as a fast response unit was proposed by Wang *et al.* (*24*) (Fig. 4, D and E).

The NK cell cluster displayed a profound change in its transcriptional signature. First, we distinguished this cluster from the closely related, but less cytotoxic ILC1 cells (in nomenclature both belonging to the group 1 ILCs) through their high expression of *Ncr1* (also known as Nkp46), *Il12rb2*, and *Eomes* (*25*, *26*). Because of their high expression of *Hmgb2*, *Zmiz1*, *Hopx*, *Itgam*, *Irf8*, and *Itagl*, we further identified this cluster as effector NK1 cells (Fig. 4F) (*27*). After combination treatment with MTP-HDL and CIs, we found increased NK cell numbers in the tumor microenvironment (Fig. 4G) accompanied by heightened cytotoxic activity, evidenced by the up-regulation of the perforin coding genes *Gzma*, *Gzmb*, and *Prf1*, each a recognized augmenter of lysosomal function (Fig. 4H) (*28*). Further analysis revealed a pronounced pro-inflammatory and activation signature, characterized by the up-regulation of *Irf8*, *Slamf7*, *Cyba*, and *Nkg7*, and a simultaneously higher expression of the chemoattractant *Ccl5*. Similar to monocytes, trained immunity can be induced in NK cells. We therefore expect alterations in their transcriptome to also stem from changes in the hematopoietic organs in which NK cells mature. Using CENCAT flow cytometry, we established glycolysis rates in NK cells. Splenic NK cells displayed a significantly higher glycolytic dependence in mice treated with MTP-HDL as compared to untreated mice, while bone marrow NK cells did not exhibit this metabolic change ($P = 0.0379$ and $P = 0.2930$; Fig. 4I and fig. S5C). Using flow cytometry, we measured the inflammatory state. We found that only combination therapy of MTP-HDL and CIs significantly increased the number of NK cells in the spleen as compared to PBS (PBS versus MTP-HDL + CI: $P = 0.0083$). Simultaneously, this treatment up-regulated the lysosomal marker Granzyme B (MTP-HDL: $P = 0.0500$; MTP-HDL + CI: $P = 0.0014$; Fig. 4J). These data collectively suggest that treatment with MTP-HDL potentiates CI therapy through the promotion of a pro-inflammatory phenotype of multiple cell types in the tumor microenvironment.

Trained immunity induction enhances myeloid-lymphoid cross-talk

T cell function can be suppressed by tumor-associated myeloid cells, impairing their antitumoral behavior. We hypothesize that as a result of the MTP-HDL checkpoint inhibition combination therapy, critical changes in the transcriptional signature of both lymphoid cells and myeloid cells improve cell-cell interactions to mount proper antitumor responses. We applied the CellChat and CellPhoneDB software packages to analyze cell-cell interactions (Fig. 5A) (*29*). While monotherapy induced some changes in the amount and nature of cell-cell interactions, we found that the combination therapy caused a much stronger increase in the number of interactions (PBS: 40 interactions; MTP-HDL + CI: 317 interactions) (Fig. 5, A and B). In untreated mice, we found interactions indicative of immunosuppression, including high osteopontin signaling (*Spp1_Cd44*). The latter is reported to inhibit T cell activation and skew macrophages toward a protumor phenotype (Fig. 5C) (*30*).

Both MTP-HDL monotherapy and CI monotherapy are associated with distinct, but minor, increases in pro-inflammatory communication. MTP-HDL treatment elevates chemokine signaling between immune cells, which is facilitated by *Ccl7_Ccr2* and *Ccl12_Ccr2* up-regulation. This is further accompanied by the costimulatory receptor ligand interaction *Tnfsf9_Tnfrsf9* (also known as *4-1Bbl*) (*31*). CI monotherapy-elevated cell-cell interaction required for lymphocyte activation. Nonetheless, these responses remain incomplete and are accompanied by remnant immunosuppressive signatures such as *Vegf* family interactions (fig. S5D). In contrast, combination treatment induces a broad pro-inflammatory signature of cell-cell interactions. This includes recruitment signals for multiple cell types such as monocytes (*Ccl2_Ccr2*), neutrophils (*Cxcl2_Cxcr2*), and NK cells (*Ccl3/4/5*, otherwise known as MIP-1α/β and RANTES). In addition, canonical inflammatory interactions including tumor necrosis factor–α (TNF-α) and interleukin-6 (IL-6) are robustly engaged. This overall pro-inflammatory state was accompanied by increased regulatory signaling, such as *April–Taci*, possibly induced by T_{reg} cells (Fig. 5C).

To further enhance our knowledge on the cell-cell signaling, we used the CellPhoneDB software to investigate interactions between myeloid and T cells. We found that in all groups (PBS, MTP-HDL, CI, and MTP-HDL + CI), T cells receive a costimulatory signal through the binding of CD28 to CD80/CD86. However, in mice treated with either checkpoint inhibition, MTP-HDL monotherapy, or the combination of both, we found a reduction of CTLA-4 binding to CD80/CD86 (Fig. 5, D and E). Therefore, it can be anticipated

Downloaded from https://www.science.org at Technische University Eindhoven on October 30, 2026

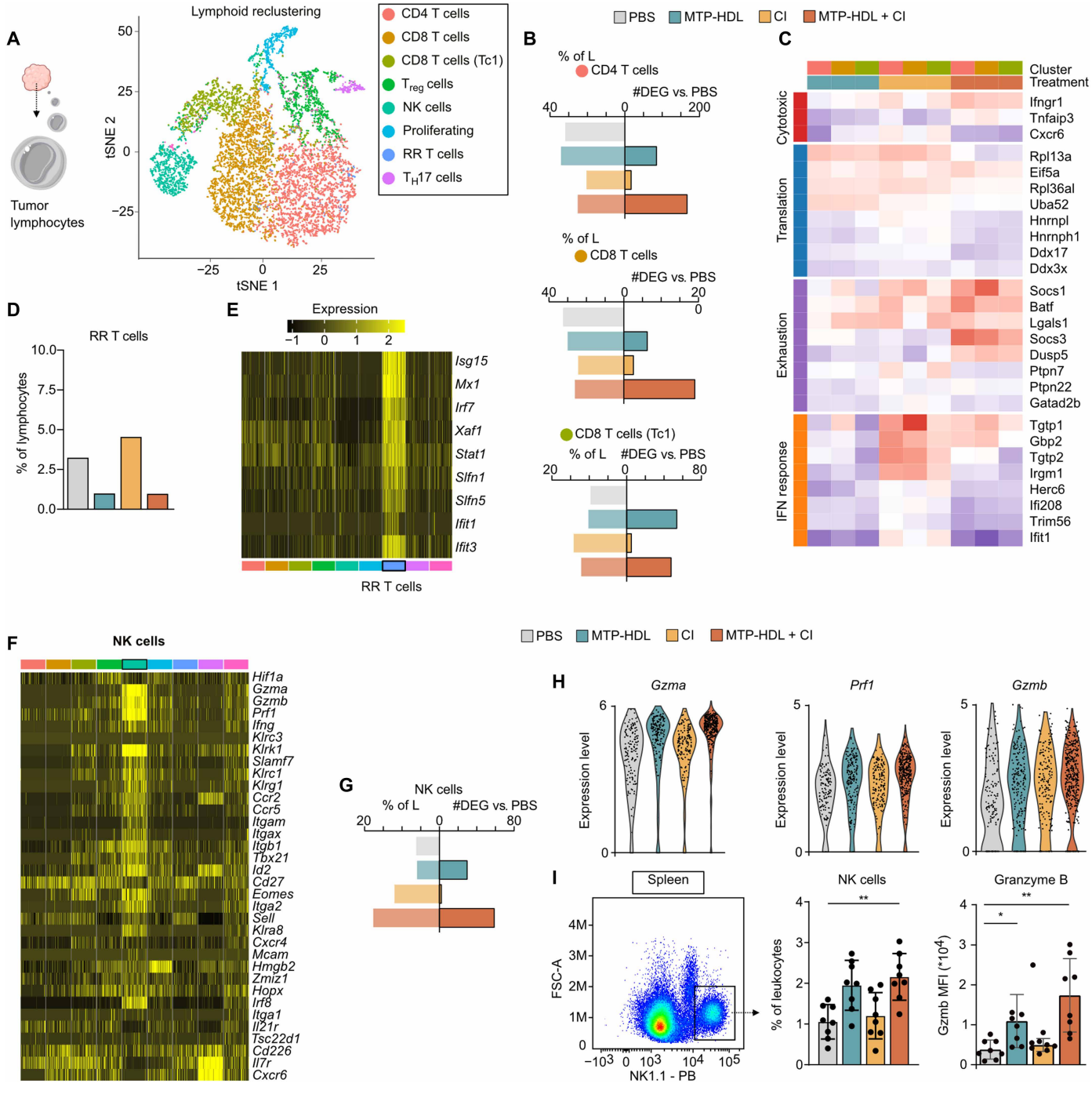

Fig. 4. NK cells are activated following MTP-HDL treatment. (**A**) This figure is mainly focused on lymphoid cells excluding B cells, accompanied by a tSNE plot displaying lymphoid reclustering in bulk. (**B**) Plots displaying the population shift and the DEGs in CD4, CD8, and CD8 Tc1 (FDR < 0.05 and fold change: 0.25 > FC < −0.25). (**C**) Heatmap displaying functional grouping of the DEGs in the macrophage cluster across all treatment groups. (**D**) Bar graph displaying the lower presence of the RR T cell group after treatments containing MTP-HDL. (**E**) Heatmap of the genes expressed by rapid response T cell group described by Wang *et al.* (*24*). Several pro-inflammatory genes are highly expressed as compared to other clusters and quiescent markers *Slfn1* and *Slfn5*. (**F**) Plot displaying the population shift and the DEGs in NK cells and a heatmap of cluster marker genes of NK cells. (**G**) Plot displaying the population shift and the DEGs in NK cells (FDR < 0.05 and fold change: 0.25 > FC < −0.25). (**H**) Violin plots of NK cell perforins *Gzma*, *Gzmb*, and *Prf1* across different treatment groups. These genes are all differentially expressed in the combination treatment group as compared to PBS (FDR < 0.05). (**I**) Flow cytometry dot plot and bar graphs highlighting the amount of splenic NK cells and Granzyme B expression. Significantly higher amount of NK cells was present in the combination treatment group, and a significantly higher expression of Granzyme B was found in treatment groups containing MTP-HDL ($n = 8$ per group). All genes mentioned are significant, defined as an adjusted P value below 0.05 and a fold change below −0.25 or above 0.25. For all panels, data are presented as means ± SD and means ± SEM for tumor growth experiments. For the tumor growth experiment, significance shown in the graph is that of the tumor growth rate. $^*P < 0.05$ and $^{**}P < 0.01$.

Downloaded from https://www.science.org at Technische University Eindhoven on October 30, 2026

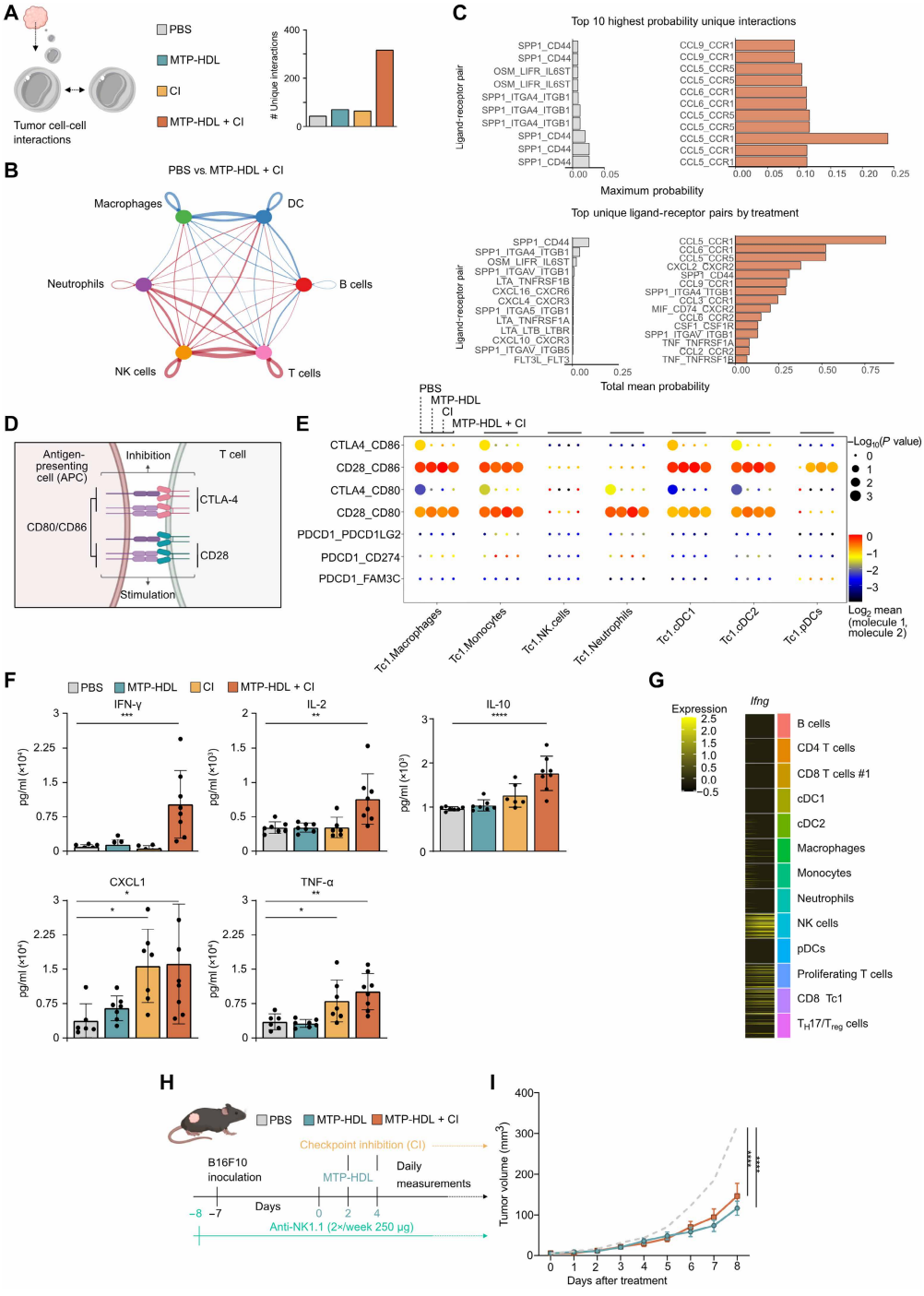

Fig. 5. Trained immunity induction enhances myeloid-lymphoid cross-talk. (**A**) CellChat analysis found combination treatment to display a higher amount of cell-cell interactions compared to PBS or both monotherapy groups. (**B**) Circle plot displaying the changes in cell-cell interactions comparing combination therapy with PBS. (**C**) Top 10 highest probability unique interactions and the top unique ligand-receptor pairs found in PBS and combination therapy. Interactions present in the PBS group are mostly of an anti-inflammatory nature, whereas the combination therapy displays pro-inflammatory interactions. (**D**) Schematic overview of the binding of CD28 to CD80/86, and CTLA-4 to CD80/86. (**E**) CellPhoneDB analysis highlighting cell-cell interaction between myeloid cells and the CD8 Tc1 effector group. Treatment stops CTLA-4 and CD80/86 interaction. (**F**) Bar graphs displaying cytokine levels of tumor lysate. Most strikingly is the higher presence of IFN-γ and IL-2 in the combination treatment group ($n = 8$ per group). (**G**) Heatmap highlighting NK cell contribution of IFN-γ production based on their *Ifny* expression level. (**H**) Schematic overview of tumor growth analysis in NK-cell–depleted mice. Depletion was achieved with 250 µg of anti-NK1.1, and mice were treated with PBS, three injections of MTP-HDL at 1.5 mg/kg, or combination therapy of MTP-HDL and CIs. (**I**) Tumor growth curves of NK cell–depleted mice C57BL/6 mice inoculated with 1×10^5 B16F10 cells. Results show significant decrease in tumor growth of mice treated with MTP-HDL; however, no significant additive effect of CI therapy is observed ($n = 10$ per group). All genes mentioned are significant, defined as an adjusted *P* value below 0.05 and a fold change below −0.25 or above 0.25. For all panels, data are presented as means ± SD. *$P < 0.05$, **$P < 0.01$, ***$P < 0.001$, and ****$P < 0.0001$.

Downloaded from https://www.science.org at Technische University Eindhoven on October 30, 2026

ERRATUM PUBLISHED 25 SEPTEMBER 2026; SEE LAST PAGE

that trained immunity induction is more effective in combination with anti–PD-1 than with anti–CTLA-4 checkpoint inhibition therapy.

Therefore, we studied cytokine concentrations in the tumor microenvironment using an electrochemiluminescence assay on the lysates of excised tumors. In these lysates, we found higher concentrations of the pro-inflammatory cytokines TNF-α and CXCL-1 in the groups containing CIs. In addition, we found that combination therapy with MTP-HDL and CI showed significantly elevated concentrations of the anti-inflammatory cytokine IL-10 ($P < 0.0001$). Most notably is the significantly higher secretion of IL-2 and interferon-γ (IFN-γ) (IL-2: $P = 0.0031$; IFN-γ: $P = 0.0005$), two pivotal cytokines in antitumor immunity, which we observed in the combination therapy regimen only (Fig. 5F and fig. S6A). To identify the source of these cytokines, we found through transcriptomic expression analyses that the elevated production of IFN-γ was largely driven by NK cells (Fig. 5G and fig. S6B). This observation sheds additional light on the way NK cells, activated by MTP-HDL, drive antitumor immunity in the tumor microenvironment.

The combined data in Figs. 4 and 5 suggest that NK cells play a crucial role in the observed antitumor effect. We performed a B16F10 tumor growth profiling experiment in mice that received an intraperitoneal injection of anti-NK1.1 antibody before treatment with either PBS, MTP-HDL monotherapy, or the combination of MTP-HDL and CIs (Fig. 5H and fig. S6D). We found that the depletion of NK cells did not affect the tumor growth inhibition induced by MTP-HDL treatment (PBS versus MTP-HDL: $P < 0.0001$; PBS versus MTP-HDL + CI: $P < 0.0001$). The NK cell depletion did nullify CI therapy's additive effect on tumor growth inhibition. We did not observe differences between MTP-HDL monotherapy and the combination with checkpoint inhibition in neither tumor size at the final day of experiment nor tumor growth rate (MTP-HDL: 116 ± 55 mm^3; MTP-HDL + CI: 146 ± 99 mm^3; $P = 0.3983$; TGR: MTP-HDL versus MTP-HDL + CI: $P = 0.7750$) (Fig. 5I).

For effective T cell activation, cytokine responses and costimulatory and coinhibitory signals need to be properly balanced. In line with this, the elevated IL-2 production facilitates cross-talk between the innate and adaptive immune responses. However, the above-mentioned transcriptional changes in monocytes are primarily relevant if they underlie functional changes. To determine this, we isolated and carboxyfluorescein diacetate succinimidyl ester (CFSE)–stained T cells from naïve C57BL/6 mice and cocultured them with monocytes isolated from murine spleens from three treatment groups. The first group was naive and received neither treatment nor tumor inoculation. The second and third group were inoculated with B16F10 cells and treated with either PBS (second group) or MTP-HDL (third group). After plating, T cells were stimulated using CD3/CD28 beads and recombinant IL-2 (Fig. 6A). We found that proliferation of activated CD4 and CD8 T cells cocultured with monocytes from nontreated tumor-bearing mice was significantly decreased as compared to naïve mice (CD4: $P = 0.0010$; CD8: $P = 0.0012$), highlighting the monocytes' immunosuppressive nature. Conversely, after treatment with MTP-HDL, we observed significantly higher proliferation of CD8 T cells compared to nontreated tumor-bearing mice ($P = 0.0393$) (Fig. 6B and fig. S6E). In this group, we did not observe significant differences in the amount of CD4 and CD8 proliferation as compared to a fully naïve mouse ($P = 0.1060$). These data suggest that functional changes in both myeloid cells and T cells are required to optimally enhance intercellular crosstalk for proper antitumor responses.

Translational tumor-agnostic immunotherapy

The above-described data collectively show that induction of trained immunity inhibits tumor growth through a pro-immune activation shift in the myeloid compartment. In turn, immunologically active myeloid cells restore T cell engagement, making CI therapy more effective. Identifying this as the principal mode of action, we conclude that MTP-HDL should be efficacious independent of the mouse strain and tumor type. To validate this assumption, we selected three syngeneic murine tumor types known to be resistant to immune CI therapy, namely, Lewis lung carcinoma (LLC), 4T1 breast cancer (4T1), and the PANC-02 pancreatic cancer (PANC-02). Through tumor growth profiling, we studied the therapeutic effects of PBS, MTP-HDL monotherapy, anti–PD-1 + anti–CTLA-4, or combined MTP-HDL. Seven days before starting the treatments, we inoculated C57BL/6 mice with 1×10^5 LLC cells and 2×10^6 PANC-02 tumor cells, while we inoculated the 1×10^5 4T1 cells in BALB/c mice. At the day of treatment initiation, we randomized mice to the different groups and performed tumor size measurements until the first mouse reached a humane end point (Fig. 6C).

In mice inoculated with LLC tumors, both therapeutic strategies containing MTP-HDL reduced the tumor growth rate relative to PBS (PBS versus MTP-HDL: $P = 0.0056$; PBS versus MTP-HDL + CI: $P < 0.0001$), with the combination therapy being superior over MTP-HDL monotherapy ($P = 0.0437$), while CI therapy alone was ineffective (PBS vesus CI: $P = 0.6149$) (Fig. 6D). These results were mirrored in 4T1 tumors, showcasing noticeable inhibitory effects for both treatments compared to PBS (PBS versus MTP-HDL: $P = 0.0064$; PBS versus MTP-HDL + CI: $P < 0.0001$). The combination therapy outperformed MTP-HDL alone ($P = 0.0149$), and the checkpoint inhibition alone did not elicit any antitumor response (Fig. 6E). Last, for PANC-02 tumors, while both MTP-HDL treatments resulted in significant growth inhibition compared to PBS (PBS versus MTP-HDL: $P = 0.0110$; PBS versus MTP-HDL + CI: $P = 0.0021$), the growth rate difference between combination therapy and MTP-HDL monotherapy was not statistically significant ($P = 0.1616$). Still, a notable difference in tumor size was evident on day 18, the study's termination point, with the combination treatment resulting in smaller tumors (MTP-HDL: 191 ± 43 mm^3; MTP-HDL + CI: 88 ± 26 mm^3; $P = 0.0002$; Fig. 6F). The data confirm our hypothesis that the induction of trained immunity serves as a therapeutic modality independent of tumor type, potentially expanding the therapeutic range of CIs to malignancies previously refractory to this type of immunotherapy.

DISCUSSION

Previously, we have shown a link between the immunosuppressive tumor microenvironment and bone marrow myeloid reprogramming in solid tumors, and we showed that the systemic induction of trained immunity overcomes local immunosuppression using MTP-HDL. In the current study, we showed that MTP-HDL therapy reshapes the immunosuppressive tumor microenvironment. It induces a more pro-inflammatory state of the myeloid cells and NK cells, and we confirmed NK cell necessity for MTP-HDL's potentiating effect on CIs. Trained immunity induction by MTP-HDL also alleviates tumor-induced, myeloid-driven T cell inhibition. Our results are in line with recent studies showing trained immunity induction to be an effective anticancer strategy (*7*, *10*, *32*). These studies underscored that molecular reprogramming of progenitor cells (*7*) is

Downloaded from https://www.science.org at Technische University Eindhoven on October 30, 2026

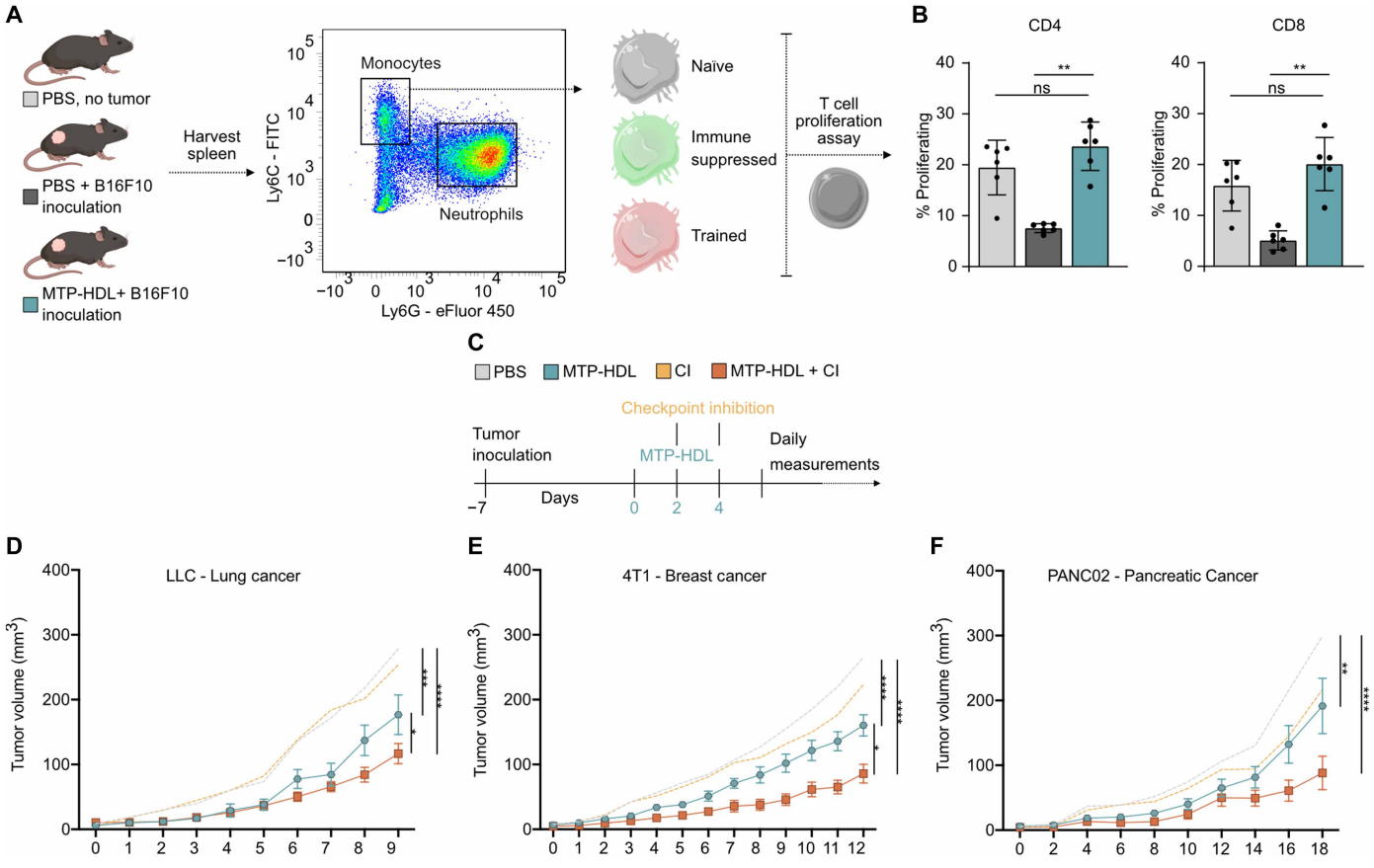

Fig. 6. Translational tumor-agnostic immunotherapy. (**A**) T cell suppression assay experimental overview. CFSE-stained naïve T cells stimulated with CD3/CD28 beads were cocultured with monocytes from either naïve mice, tumor-bearing mice, or tumor-bearing mice that have received MTP-HDL treatment. (**B**) Bar plots displaying the percentage of proliferating CD4 or CD8 cells after the above described treatment regimen. Monocytes from untreated tumor-bearing mice significantly hampered T cell proliferation of both CD4 and CD8 T cells, while monocytes from treated tumor-bearing mice regained their effectiveness ($n = 6$ per group). (**C**) Schematic overview of treatment regimen. Mice were treated with either PBS, three injections of MTP-HDL at 1.5 mg/kg, anti–CTLA-4 and anti–PD-1 at 200 μg each, or combination therapy of MTP-HDL and CIs. (**D** to **F**) Tumor growth curve of (i) C57BL/6 mice inoculated with 1×10^5 Lewis lung carcinoma (LLC) cells, (ii) Balb/c mice inoculated with 1×10^5 4T1 breast cancer cells, and (iii) C57BL/6 mice inoculated with 2×10^6 PANC-02 pancreatic cancer cells. (D) Both therapeutic strategies containing MTP-HDL reduced the tumor growth rate relative to PBS, with the combination therapy being superior over MTP-HDL monotherapy. (E) Both therapeutic strategies containing MTP-HDL reduced the tumor growth rate relative to PBS, with the combination therapy being superior over MTP-HDL monotherapy. (F) Both MTP-HDL treatments resulted in significant growth inhibition; yet, the difference in growth rate between the combination therapy and MTP-HDL monotherapy was not statistically significant. However, the tumor in the combination therapy was significantly smaller at the last day of experiment as compared to MTP-HDL monotherapy. For all panels, data are presented as means ± SD and means ± SEM for tumor growth experiments. For the tumor growth experiment, significance shown in the graph is that of the tumor growth rate. *$P < 0.05$, **$P < 0.01$, ***$P < 0.001$, and ****$P < 0.0001$. FITC, fluorescein isothiocyanate.

an integral part of trained immunity, resulting in trained myelopoiesis that gives rise to more immunologically responsive monocytes, macrophages (*6*), NK cells (*33*), and neutrophils (*32*).

MTP-HDL engages NOD2 on myeloid cells and progenitor cells inducing chromatin accessibility at inflammatory loci alongside a durable shift to Akt-mTOR-Hif1 driven glycolysis (*34*). We quantitatively evaluated enhanced glycolytic activity following MTP-HDL treatment by studying ^{18}F-FDG uptake in the bone marrow and spleen using ex vivo gamma counting of tissues from euthanized C57BL/6 mice. We found the increased ^{18}F-FDG uptake in these organs to correlate with GLUT-1 expression in the myeloid cells, highlighting that the metabolism of these cells has shifted which is indicative of trained immunity (*10*, *19*). Mirroring the elevated GLUT-1 expression of myeloid cells in the bone marrow and spleen, we found a strikingly higher GLUT-1 expression in myeloid cells present in the tumor microenvironment. Collectively, these data indicate that immunosuppressive myeloid cells populating the tumor microenvironment are replaced by infiltrating trained monocytes originating from the hematopoietic organs.

Galvanized by the abovementioned functional changes caused by systemic trained immunity induction, we profiled the tumor microenvironment using scRNA-seq. First, we found that macrophages present in the tumor have a more pronounced pro-inflammatory phenotype upon induction of trained immunity using MTP-HDL. Second, after MTP HDL treatment, we observed the presence of two myeloid subclusters with differentiating and pro-inflammatory characteristics, which is in line with the concept that the influx of trained monocytes gradually replaces immunosuppressant cells residing in the tumor microenvironment. Last, flow cytometric analysis revealed that in splenic macrophages CD206 is down-regulated after

Downloaded from https://www.science.org at Technische University Eindhoven on October 30, 2026

either MTP-HDL and CI monotherapies, indicative of a reduced inflammatory state. Conversely and critical for the antitumorigenic effects, the combination therapy with MTP-HDL and checkpoint inhibition caused a pronounced pro-inflammatory signature in splenic monocytes, as determined by the elevated iNOS expression.

The induction of trained immunity in combination with checkpoint blockade simultaneously leads to the proliferation and activation of effector NK cells, an effect not caused by either monotherapies. These effector NK cells also originate from the hematopoietic organs, where their numbers have increased, and the expression of the pro-inflammatory marker Granzyme B is up-regulated. Several factors likely underly this shift in NK cells. The engagement of NOD2 by MTP-HDL can train NK cells directly and indirectly. Direct training of NK cells and their progenitors expands $KLRG1^+$ NK cells with augmented IFN-γ output (*35*). Indirectly, the systemic induction of trained immunity leads to NK cell activation by trained DCs and macrophages and the release of pro-inflammatory cytokines allowing for cytokine driven memory (*36*, *37*). Another contributing factor is the down-regulation of PD-1 in NK cells (*38*). Collectively, the activation of NK cells and a myeloid repopulation of the tumor microenvironment are the critical forces driving the combination therapy's antitumorigenic effects. This phenomenon is exemplified by the NK cells' elevated IFN-γ production, which provides an additional pro-inflammatory stimulus to the myeloid cells present in the tumor microenvironment.

Upon identifying trained myeloid and activated NK cell populations, we further elucidated the mechanism through which MTP-HDL therapy potentiates checkpoint inhibition. We found trained innate immune cells' to effectively stimulate T cell activation, overcoming their suppressed function (signal 1 in T cell activation). Furthermore, the NK cells create a cytokine environment more hospitable for T cell activation (signal 3), while CD28 costimulation (signal 2), as observed in our CellPhoneDB analysis, in conjunction with anti–PD-1 and anti–CTLA-4 immunotherapy, facilitates effective anticancer T cell immunity (*39*). The presence of IL-10 could hamper further inflammation. Previous studies show IL-10 signaling blockade increases effectiveness of another NOD2 agonist (*40*). In line with our findings that the immunosuppression is myeloid cell–driven in the B16F10 melanoma model, MTP-HDL treatment also potentiates immune CI therapy in other tumor mouse models, including 4T1 breast cancer, LLC lung cancer, and PANC-02 pancreatic cancer.

The present study has some limitations. The current study focused on murine experimental models, and future studies must be performed to demonstrate the approach's effectiveness in patients with cancer. It is important to realize that patients often receive chemotherapeutic treatment, which compromises myelopoiesis. Because the induction of trained immunity relies on a functional innate immune response, this may limit our approach's efficacy. In the current study, we focused on myeloid cells in the tumor microenvironment. As it is expected that myeloid cell programs are changed in other organs, further studies are warranted to map potential immune-mediated side effects. Our work implies that pharmacologically inducing trained immunity can make current immunotherapy strategies more effective for many types of cancers, including those that are now not treatable with checkpoint inhibition. Future studies should address the remaining challenges by investigating MTP-HDL nanobiologics in other experimental models, including nonhuman primates. Ultimately, the development of GMP-level trained immunity-inducing immunotherapies, including MTP-HDL, is required to perform clinical studies and demonstrate the effectiveness of this approach in human cancer.

MATERIALS AND METHODS

Inbred mice strains

C57BL/6 and BALB/c mice were purchased from The Jackson Laboratory and Charles River respectively. All animal experiments were performed in accordance with Icahn School of Medicine at Mount Sinai Institutional Animal Care and Use Committee (IACUC), Radboud and VU University Medical Center Dierexperimentencommissie (DEC) guidelines as well as Dutch requirements and laws on animal experimentation. Mice were co-housed and allowed to acclimate to the housing facility for at least 1 week. All mice had free access to food and water and were randomly assigned to experimental groups.

Tumor inoculation and treatment regimen

7-week-old female C57BL/6 and BALB/c mice were purchased from The Jackson Laboratory and Charles River respectively. For B16F10, LLC and 4T1 tumor experiments, 1 × 105 tumor cells in 100 μl PBS supplemented with 0.5% fetal bovine serum (FBS) were injected subcutaneously in the flank on day −7. For PANC-02, 2 × 106 tumor cells in 100 μl PBS supplemented with 0.5% fetal bovine serum (FBS) were injected subcutaneously in the flank on day −7. For NK cell depletion mice were injected with 250 μg of anti-NK1.1 1 day before B16F10 inoculation and twice weekly for the duration of experiment. On day 0, mice were randomized and treatment began. Treatment groups consisted of a control PBS group, a MTP-HDL treatment group that received a 1.5 mg/kg intravenous injection (dose calculated on the amount of MDP) on day 0, 2, and 4, a checkpoint inhibitor group and a combination treatment group that received both checkpoint inhibitors and MTP-HDL. The checkpoint inhibitor treated mice received an intraperitoneal injection twice a week using doses of 200 μg anti-CTLA-4 (clone, 9H10, BioXcell) and/or 200 μg anti-PD-1 (clone, RMP1-14, BioXcell). Treatment started at day 2 and continued until the end of the experiment, for analysis experiments that ended at day 5 mice received checkpoint inhibitor therapy at day 2 and day 4. Tumors were measured daily by caliper and tumor volume was calculated as (width × width × height) × 0.52 for tumor growth studies. At time of sacrifice for analysis, mice were euthanized using CO2 and underwent subsequent cervical dislocation.

Cell lines (B16F10, 4T1, LLC, and PANC-02)

B16F10 murine melanoma cells and Lewis Lung carcinoma cells were cultured in Dulbecco's modified Eagle's medium (DMEM) (Gibco) supplemented with 10% FBS and 1% penicillin/streptomycine (P/S). 4T1 breast cancer cells and PANC-02 pancreatic cancer cells were cultured in Roswell Park Memorial Institute medium 1640 (RPMI-1640) (Gibco) supplemented with 10% FBS, 1% P/S. Isolated T cells were cultured in RPMI-1640 (Gibco) supplemented with 10% FBS, 1% P/S, 1mM Sodium Pyruvate (Gibco), L-glutamine (Gibco), and MEM Non-essential amino acids (Milipore Sigma) and 55 μM β-mercaptoethanol (Gibco).

Materials

1,2-dimyristoyl-*sn*-glycero-3-phosphocholine (DMPC) was obtained from Avanti Lipids. apoA1 was purified in house from human HDL obtained from Biosource Technology. All dyes were obtained from Thermo Fisher Scientific. apoA1 was isolated from human HDL

Downloaded from https://www.science.org at Technische University Eindhoven on October 30, 2026

concentrates and purified as previously reported (*38*). All other chemicals were obtained from Sigma-Aldrich. Vivaspin tubes were obtained from Sartorius Biotech, and PD-10 columns were purchased from General Electric (Sephadex G-25 M). A 150 V/T ultrasonic homogenizer working at 70% power output was used for tip sonication. Dynamic light scattering measurements were performed on a Brookhaven Instrument Corporation ZetaPals analyzer. Size exclusion chromatography (SEC) radio–high-performance liquid chromatography (HPLC) analyses were performed on a Shimadzu system equipped with a Superdex 10/300 SEC column using a flow rate of 1 ml/min and demiwater as the eluent. A Lablogic Scan-RAM radio-TLC/HPLC detector was used. Dialysis experiments were performed using 10-kDa Slide-a-Lyzer dialysis cassettes from Thermo Fisher Scientific.

Formulating the nanobiologics

DMPC (5 mg, 7.37 μmol), cholesterol (0.57 mg, 1.47 μmol), and MTP-PE (mifamurtide) (0.91 mg, 0.74 μmol) were dissolved in chloroform (2 ml) and placed in a 20-ml vial. Chloroform was evaporated under vacuum to form a thin lipid film, to which apoA1 (2 mg) and PBS (5 ml) were added, and the mixture was sonicated using an ultrasonic bath for 5 min, followed by incubation at 37°C for 20 min. The opaque solution was sonicated using a tip sonicator for 30 min while cooling in an ice-water bath. The transparent solution was transferred to a 10-kDa MWCO Vivaspin tube and centrifuged at 4000 rpm at 4°C until a volume of ~1 ml remained. PBS (1 ml) was added, and the tube was again centrifuged until 1 ml remained; this was repeated twice. The resulting solution was filtered using a 0.22-μm PES syringe filter to obtain the finished MTP-HDL particles. For the particles with other DMPC and MTP or cholesterol molar ratios, the same method was used with the corresponding amounts of mifamurtide or cholesterol incorporated in the lipid mix.

Gamma counting experiments

For ^{18}FDG /PET, tumor-bearing C57BL/6 mice were fasted for 8 hours before injection. ^{18}F-FDG (13.2 ± 1.0 MBq, $n = 6$ to 8, in 100 μl of PBS solution) was administered via tail vein and allowed to circulate for 30 min before PET-CT imaging. Immediately after, animals were euthanized and perfused with PBS. Tissues of interest (spleen, blood, tumor, lymph nodes, and femurs) were collected, blotted, and weighed before radioactivity counting on a Wizard2 2480 automatic gamma counter (PerkinElmer). Radioactivity values were corrected for decay and normalized to tissue weight to express radioactivity concentration as percentage injected dose per gram (%ID/g).

Preparing single-cell suspensions

Blood was collected by cardiac puncture, and mice were subsequently perfused with 20 ml of cold PBS following harvesting of spleen, tumor, and femurs. Spleens were mashed, filtered through a 70-μm cell strainer (BD Falcon), incubated with red blood cell (RBC) lysis buffer (BioLegend) for 4 min, and washed with PBS containing 0.5% fetal bovine serum (FBS). Bone marrow was flushed out of the femur with PBS, filtered through a 70-μm cell strainer (BD Falcon), incubated with RBC lysis buffer (BioLegend) for 30 s, and washed with PBS containing 0.5% FBS. Tumors were digested for 60 min at 37°C using digestion buffer consisting of deoxyribonuclease I (DNase I) (40 U/ml; Sigma-Aldrich) and hyaluronidase (60 U/ml; Sigma-Aldrich) in RPMI medium containing 5% FBS. After straining through a 70-μm cell strainer (BD Falcon), cells were incubated with RBC lysis buffer (BioLegend) for 4 min and washed with PBS containing 0.5% FBS. Live cells were isolated from digested tumors by the Dead Cell Removal Kit (Miltenyi), and tumor-infiltrating leukocytes were isolated by positive selection using mouse CD45 (tumor-infiltrating leukocyte) MicroBeads (Miltenyi) both following the manufacturer's instructions. Cells were subsequently washed in PBS and resuspended in 200 μl of a 1:250 solution of ZombieNIR and incubated at room temperature in the dark for 20 min. After this, cells were washed with fluorescence-activated cell sorting (FACS) buffer and subsequently resuspended in 100 μl of FACS buffer for staining.

GLUT-1 flow cytometry

After preparation of single-cell suspensions, cells were subsequently stained with the following cell surface monoclonal antibodies: anti-CD19 (clone 6D5), anti-CD90.2 (clone 53-2.1), anti-CD11b (clone M1/70), anti-Ly6G (clone 1A8-Ly6g), anti-Ly6C (clone 1A8), and anti-CD115 (clone T38-320). All antibodies were added at titrated concentrations for 30 min at 4°C. After 1 wash with FACS buffer, cells were fixated and permeabilized using Foxp3/Transcription Factor Staining Buffer Set (Thermo Fisher Scientific). After permeabilization, cells were stained for intracellular markes with the following monoclonal antibodies: anti-GLUT1 (clone EPR3915) for 1 hour at room temperature. After one wash with permeabilization buffer, cells were resuspended in FACS buffer. Cells were processed using the BD LSRFortessa flow cytometer (BD Bioscience).

CENCAT flow cytometry

CENCAT analysis was performed as described in the seminal paper on this technique (*39*). After preparation of single-cell suspensions, cells were counted and resuspended to a concentration of 10×10^6 cells/ml. Cells were plated and treated with either dimethyl sulfoxide, 2-deoxy-D-glucose to inhibit glucose metabolism, oligomycin to inhibit mitochondrial adenosine 5′-triphosphate synthesis, or both. Cells were subsequently treated with βES noncanonical amino acid (ncAA) (500 μM) and incubated for 30 min at 37°C/5% CO_2. Cells were subsequently washed and stained with ViaKrome 808 (Beckman Coulter). Cells were then fixated (2% formaldehyde) and permeabilized using 1X permeabilization buffer (Invitrogen). Following permeabilization buffer, ncAAs were labeled through copper(I)-catalyzed azide-alkyne cycloaddition using a reaction mix of click buffer (0.5 mM Cu(II)SO_4, 10 mM sodium ascorbate, 2 mM THPTA, and 0.5 μM AF488 Azide Plus) and were incubated for 30 min at room temperature (RT). After this, cells were washed and resuspended in flow buffer. Cells were stained with anti-Ly6C (fluorescein isothiocyanate), anti-Ly6G (allophycocyanin-Cy7), anti-NK1.1 (Spark Red 718), CD11b (eFluor 506), CD45 (PerCP), Ly-6A/E (Sca-1) [phycoerythrin (PE)], CD117 (c-kit) (BV785), CD11c (PE-Cy7), and F4/80 (PE/Dazzle 594). Cells were washed 1× with FACS buffer after staining and acquired on a CytoFLEX LX cytometer (Beckman Coulter). Cells were analyzed using OMIQ software (Dotmatics), and the glycolytic dependence was calculated as described by Argüello *et al.* (*40*)

Tumor Aurora flow cytometry

After the preparation of single-cell suspensions, cells were subsequently stained with the following cell surface monoclonal antibodies: anti-CD45 (clone 30-F11), anti-CD19 (clone 1D3), anti-CD8 (clone 53–6.7), anti-CD4 (clone GK1.5), anti-NK1.1 (clone PK136), anti–PD-1 (clone RMG1-1), anti-Ly6G (clone 1A8), anti-Ly6C (clone HK1.4), anti-F4/80 (clone BM8), anti-CD11b (clone M1/70), anti-CD90.2 (clone 30-H12), anti-CD11c (clone HL3), anti–major

Downloaded from https://www.science.org at Technische University Eindhoven on October 30, 2026

histocompatibility complex II (clone M5/114.15.2), anti-CXCR3 (clone CXCR3-173), anti–Tim-3 (clone RMT2-23), anti–Lag-3 (clone C9B7W), anti–CCR-2 (clone 475301), and anti–T cell receptor γ/δ (clone GL3). All antibodies were added at titrated concentrations for 30 min at 4°C. After one wash with FACS buffer, cells were fixated and permeabilized using Foxp3/Transcription Factor Staining Buffer Set (Thermo Fisher Scientific). After permeabilization, cells were stained for intracellular markers with the following monoclonal antibodies: anti-CD206 (clone C068C2), anti-Nos2 (clone W16030C), anti–Ki-67 (clone 16A8), anti-Granzyme B (clone QA16A02), and anti-FoxP3 (clone 150D) for 1 hour at room temperature. After one wash with permeabilization buffer, cells were resuspended in FACS buffer. All data were acquired on an 5 L Aurora flow cytometer (Cytek Biosciences).

T cell suppression

Spleens were dissected, filtered into a single-cell suspension, and depleted of RBCs using RBC lysis buffer (BioLegend) for 4 min. T cells were isolated from the spleen using the mouse Pan T Cell Isolation Kit II (Miltenyi) according to the manufacturer's instructions. Isolated T cells were washed once with PBS and resuspended at 1×10^6/ml in staining buffer [0.01% bovine serum albumin (BSA) in PBS]. T cells were stained with the CellTrace CFSE Cell Proliferation Kit (Thermo Fisher Scientific) using 5 μM dye per 1×10^6 cells and incubated in a 37°C water bath for 20 min. Last, T cells were washed and resuspended at 1×10^6/ml in RPMI 1640 with Hepes + L-glutamine (Gibco, 22400-105) complete medium containing 10% FBS (Gibco), 1X nonessential amino acids (Gibco), penicillin (100 U/ml)–streptomycin (100 μg/ml) (Gibco), 1 mM sodium pyruvate (Gibco), and 55 μM β-mercaptoethanol (Gibco). CFSE-labeled T cells were plated (10×10^4 cells per well) in a U-bottom 96-well plate (VWR, 10062-902) and activated with CD3/CD28 microbeads (BioLegend). For myeloid cell sorting, splenocytes were incubated with anti-CD19 (clone 6D5), anti-CD90.2 (clone 53-2.1), anti-CD11b (clone M1/70), anti-Ly6G (clone 1A8-Ly6g), and anti-Ly6C (clone 1A8). All antibodies were added at titrated concentrations for 30 min at 4°C. Subsequently cells were washed and resuspended in 1 ml of FACS buffer for sorting on a FACSAria Sorter (BD Biosciences). $CD11b^+Ly6C^+$ cells were collected in 15-ml Falcon tubes containing complete T cell medium without β-mercaptoethanol. Sorted $CD11b^+Ly6C^+$ monocytes from wild-type mice were added to T cells in 1:1 ratio (0.5×10^5 T cells: 0.5×10^5 $CD11b^+Ly6C^+$ cells). After 3 days of culture, cells were collected and blocked with anti-mouse CD16/32 (BioLegend) and stained with Zombie Live/Dead Dye (BioLegend) and fluorescent-conjugated antibodies: anti-CD4 (clone RM4-5), and anti-CD8 (clone 53-6.7). Single-stained samples and fluorescence minus one controls were used to establish photomultiplier tube voltages, gating, and compensation parameters. Cells were processed using the BD LSRFortessa flow cytometer (BD Bioscience) and analyzed using FlowJo software (Tree Star Inc).

Cytokine concentrations tumor lysates

Excised B16F10 tumors (the day after last MTP-HDL injection) were weighed and digested for 60 min at 37°C using digestion buffer consisting of DNase I (40 U/ml; Sigma-Aldrich), hyaluronidase (60 U/ml; Sigma-Aldrich) in RPMI medium containing 5% FBS. After digestion, tumors were strained through a 70-μm cell strainer (BD Falcon). Cells were spinned down at 400*g* and resuspended in 5 ml of T-Per Lysis Buffer (Thermo Fisher Scientific) with complete protease inhibitor cocktail (Roche AppliedScience) per gram of tissue. After 5 min, the suspension was centrifuged for 5 min at 10,000*g* after which tumor the lysate was collected. Lysates were aliquoted and stored at −80°C until analysis. Tumor lysate cytokine concentrations were measured using an electrochemiluminescence assay. A V-PLEX Proinflammatory Panel 1 mouse kit (Meso Scale Diagnostics) was used to quantify IFN-γ, IL-1β, IL-2, IL-4, IL-5, IL-6, IL10, IL12p70, KC/GRO (CXCL1), and TNF. Data were acquired using a MESO QuickPlex SQ 120 plate reader (Meso Scale Diagnostics) and presented as picogram cytokine per ml tumor lysate.

scRNA-seq tumor-infiltrated $CD45^+$ cells

B16F10 tumors were isolated, and the remaining fat and veins were removed from the tumors. Tumors were chopped and digested in an enzyme solution containing collagenase type I (3.6 g/liter; Sigma-Aldrich), hyaluronidase (0.15 g/liter; Sigma-Aldrich), and DNase I (Invitrogen) in RPMI 1640 (Thermo Fisher Scientific) with 5% fetal calf serum (FCS) and 1% penicillin/streptomycin (Thermo Fisher Scientific) and incubated at 37°C for 30 min. Digested tumors were poured through a 70-μm cell strainer (Falcon). Eight pools (2×4 treatment groups) were created, and each pool consisted of five tumors per pool. Samples were centrifuged at 1300 rpm at 4°C for 10 min. Erythrocytes were lysed by incubating the samples with erythrocyte lysis buffer [155 mM NH_4Cl, 10 mM $KHCO_3$, and 0.1 mM EDTA in PBS (pH 7.4)] for 5 min at 4°C. Next, samples were washed with PBS. Subsequently, nonspecific antibody binding was inhibited using anti-CD16/CD32 (eBioscience) for 15 min at RT. Cells were labeled with anti-CD45 (1:400, 20 min, RT, BioLegend). Before sorting, cells were poured through a 50 μM filter, and cells were labeled using 7-AAD viability staining solution (1:1000; eBioscience). About 60,000 living $CD45^+$ cells were sorted per sample using a FACSAria III (BD Biosciences) and an 85-μm nozzle. Sorted cells were collected in tubes containing RPMI 1640 with 20% FCS. Sorted cells were centrifuged (1300 rpm, 4°C, 10 min) and resuspended in PBS + 0.04% BSA. Per sample, 16,500 sorted cells were used to construct a barcoded library using a Chromium Controller (10x Genomics). Libraries were constructed according to the manufacturers' instructions (Single Cell 3′ v3 protocol, 10x Genomics) and sequenced on an Illumina HiSeq4000 platform.

Histology

Tumors were excised and placed in 10% buffered formalin phosphate for 24 hours at 4°C; afterward, tumors were washed, and the formalin solution was replaced with 70% ethanol in aqueous for storage at 4°C. Slides were prepared after tissues were fixed and embedded in paraffin. Blank slides (3 μm) were used for immunohistochemistry (IHC). IHC was completed through the Discovery Ultra Automated Immunostainer using the RUO Discovery Universal Procedure, a system that allows for the automated baking, deparaffinization, and cell conditioning of the samples. Semiautomatic staining was performed using either CD3 (Cell Signaling Technology) at a dilution of 1:500 or CD11b (Cell Signaling Technology) at a dilution of 1:4000 for 60 min. As the secondary antibody, Discovery OMNIMap anti-rabbit-HRP (Roche) was used and signal was obtained using Discovery ChromoMap DAB RUO (Roche) (brown signal). Tissues were also counterstained with hematoxylin (in blue). Images of the slides were taken via bright-field microscopy using Keyence All-in-One Fluorescence Microscope BZX-810.The photographs were stitched using the accompanying BZ-H4AXD/Advanced Observation Module Image Analyzer software.

Downloaded from https://www.science.org at Technische University Eindhoven on October 30, 2026

ERRATUM PUBLISHED 25 SEPTEMBER 2026; SEE LAST PAGE

Quantification and statistical analysis

RNA sequencing analysis

Data were analyzed using the pipeline Cell Ranger count (v3.1.0, 10x Genomics) with the *Mus musculus* genome (mm10-3.0.0) and Seurat (v4.3.0) (*41*) in an R (v4.2.1) environment. Cells were filtered using the following cutoffs: nFeature_RNA > 200, nFeature_RNA < 7500, and percent.mito < 0.15. Libraries were integrated using the Seurat functions FindIntegrationAnchors() and IntegrateData() with dims = 1:20. Unsupervised clustering was performed to create clusters of cells (dims = 1:20, resolution = 0.5). Myeloid and lymphoid cells were reclustered respectively (myeloid cells: dims = 1:20, resolution = 0.25 and lymphoid cells: dims = 1:30, resolution = 0.25) and further annotated via cluster marker identification and expression levels for each of the clusters and confirmed by literature. DEGs were identified using FindMarkers() with test.use = MAST. Gene Ontology (GO) pathway enrichment analysis was performed using the function enrichGO() with ont = "BP" of the R package clusterprofiler (v4.4.4) (*42*). The package CellphoneDB (v3.1.0) (*43*) was run using Python (v3.8.0) per treatment group using the CellphoneDB statistical method. In addition, we used CellChat (v2.1.2) in R (v4.2.1) with Seurat (v4.3.0). Communication probabilities were calculated using the CellChat mouse database (*40*).

Histology analysis

Histological analysis was completed using Fiji ImageJ. Images were color-deconvoluted for hematoxylin and eosin DAB, and the highest contrast images were taken for further analysis. Seven sections of the tumor were taken to ensure complete coverage, while avoiding necrotic sections. A minimum color threshold for each individual section was set to encompass and determine the stained area. This area was then then compared to the total area of the section by increasing the color threshold to include all cells within the boundaries.

Statistical analysis

All data are presented as means ± SD except for tumor growth experiments where means ± SEM is presented. Number (n) and type (biological or technical) of replicates are indicated in the figure legends. Tumor growth curves were analyzed by growth rate analysis as described by Hathers *et al.* (*44*). Data were tested using a Kurskall-Wallis test, followed by Dunn's post hoc comparison (to test multiple groups) in GraphPad Prism version 7.0 software, as indicated in the figure legends. P values < 0.05 were considered significant, with levels of significance as follows: $^{*}P < 0.05$, $^{**}P < 0.01$, $^{***}P < 0.001$, and $^{****}P < 0.001$; ns, not significant.

Supplementary Materials

This PDF file includes:

Figs. S1 to S6

REFERENCES

1. D. I. Gabrilovich, S. Ostrand-Rosenberg, V. Bronte, Coordinated regulation of myeloid cells by tumours. *Nat. Rev. Immunol.* **12**, 253–268 (2012).
2. V. Kumar, S. Patel, E. Tcyganov, D. I. Gabrilovich, The nature of myeloid-derived suppressor cells in the tumor microenvironment. *Trends Immunol.* **37**, 208–220 (2016).
3. K. Rabold, M. Zoodsma, I. Grondman, Y. Kuijpers, M. Bremmers, M. Jaeger, B. Zhang, W. Hobo, H. J. Bonenkamp, J. H. W. de Wilt, M. J. R. Janssen, L. A. M. Cornelissen, I. C. H. van Engen-van Grunsven, W. J. M. Mulder, J. W. A. Smit, G. J. Adema, M. G. Netea, Y. Li, C. J. Xu, R. T. Netea-Maier, Reprogramming of myeloid cells and their progenitors in patients with non-medullary thyroid carcinoma. *Nat. Commun.* **13**, 6149 (2022).
4. M. G. Netea, L. A. Joosten, E. Latz, K. H. Mills, G. Natoli, H. G. Stunnenberg, L. A. O'Neill, R. J. Xavier, Trained immunity: A program of innate immune memory in health and disease. *Science* **352**, aaf1098 (2016).
5. M. G. Netea, J. Quintin, J. W. M. van der Meer, Trained immunity: A memory for innate host defense. *Cell Host Microbe* **9**, 355–361 (2011).
6. J. Kleinnijenhuis, J. Quintin, F. Preijers, L. A. Joosten, D. C. Ifrim, S. Saeed, C. Jacobs, J. van Loenhout, D. de Jong, H. G. Stunnenberg, R. J. Xavier, J. W. van der Meer, R. van Crevel, M. G. Netea, Bacille Calmette-Guérin induces NOD2-dependent nonspecific protection from reinfection via epigenetic reprogramming of monocytes. *Proc. Natl. Acad. Sci. U.S.A.* **109**, 17537–17542 (2012).
7. I. Mitroulis, K. Ruppova, B. Wang, L. S. Chen, M. Grzybek, T. Grinenko, A. Eugster, M. Troullinaki, A. Palladini, I. Kourtzelis, A. Chatzigeorgiou, A. Schlitzer, M. Beyer, L. A. B. Joosten, B. Isermann, M. Lesche, A. Petzold, K. Simons, I. Henry, A. Dahl, J. L. Schultze, B. Wielockx, N. Zamboni, P. Mirtschink, U. Coskun, G. Hajishengallis, M. G. Netea, T. Chavakis, Modulation of myelopoiesis progenitors is an integral component of trained immunity. *Cell* **172**, 147–161.e12 (2018).
8. M. Divangahi, P. Aaby, S. A. Khader, L. B. Barreiro, S. Bekkering, T. Chavakis, R. van Crevel, N. Curtis, A. R. DiNardo, J. Dominguez-Andres, R. Duivenvoorden, S. Fanucchi, Z. Fayad, E. Fuchs, M. Hamon, K. L. Jeffrey, N. Khan, L. A. B. Joosten, E. Kaufmann, E. Latz, G. Matarese, J. W. M. van der Meer, M. Mhlanga, S. Moorlag, W. J. M. Mulder, S. Naik, B. Novakovic, L. O'Neill, J. Ochando, K. Ozato, N. P. Riksen, R. Sauerwein, E. R. Sherwood, A. Schlitzer, J. L. Schultze, M. H. Sieweke, C. S. Benn, H. Stunnenberg, J. Sun, F. L. van de Veerdonk, S. Weis, D. L. Williams, R. Xavier, M. G. Netea, Trained immunity, tolerance, priming and differentiation: Distinct immunological processes. *Nat. Immunol.* **22**, 2–6 (2021).
9. B. Priem, M. M. T. van Leent, A. J. P. Teunissen, A. M. Sofias, V. P. Mourits, L. Willemsen, E. D. Klein, R. S. Oosterwijk, A. E. Meerwaldt, J. Munitz, G. Prevot, A. Vera Verschuur, S. A. Nauta, E. M. van Leeuwen, E. L. Fisher, K. A. M. de Jong, Y. Zhao, Y. C. Toner, G. Soultanidis, C. Calcagno, P. H. H. Bomans, H. Friedrich, N. Sommerdijk, T. Reiner, R. Duivenvoorden, E. Zupancic, J. S. Di Martino, E. Kluza, M. Rashidian, H. L. Ploegh, R. M. Dijkhuizen, S. Hak, C. Perez-Medina, J. J. Bravo-Cordero, M. P. J. de Winther, L. A. B. Joosten, A. van Elsas, Z. A. Fayad, A. Rialdi, D. Torre, E. Guccione, J. Ochando, M. G. Netea, A. W. Griffioen, W. J. M. Mulder, Trained immunity-promoting nanobiologic therapy suppresses tumor growth and potentiates checkpoint inhibition. *Cell* **183**, 786–801.e19 (2020).
10. S. C. Cheng, J. Quintin, R. A. Cramer, K. M. Shepardson, S. Saeed, V. Kumar, E. J. Giamarellos-Bourboulis, J. H. Martens, N. A. Rao, A. Aghajanirefah, G. R. Manjeri, Y. Li, D. C. Ifrim, R. J. Arts, B. M. van der Veer, P. M. Deen, C. Logie, L. A. O'Neill, P. Willems, F. L. van de Veerdonk, J. W. van der Meer, A. Ng, L. A. Joosten, C. Wijmenga, H. G. Stunnenberg, R. J. Xavier, M. G. Netea, mTOR- and HIF-1α-mediated aerobic glycolysis as metabolic basis for trained immunity. *Science* **345**, 1250684 (2014).
11. A. J. Freemerman, A. R. Johnson, G. N. Sacks, J. J. Milner, E. L. Kirk, M. A. Troester, A. N. Macintyre, P. Goraksha-Hicks, J. C. Rathmell, L. Makowski, Metabolic reprogramming of macrophages: Glucose transporter 1 (GLUT1)-mediated glucose metabolism drives a proinflammatory phenotype. *J. Biol. Chem.* **289**, 7884–7896 (2014).
12. F. Vrieling, H. J. P. van der Zande, B. Naus, L. Smeehuijzen, J. I. P. van Heck, B. J. Ignacio, K. M. Bonger, J. Van den Bossche, S. Kersten, R. Stienstra, CENCAT enables immunometabolic profiling by measuring protein synthesis via bioorthogonal noncanonical amino acid tagging. *Cell. Rep. Methods* **4**, 100883 (2024).
13. J. Pillay, I. den Braber, N. Vrisekoop, L. M. Kwast, R. J. de Boer, J. A. Borghans, K. Tesselaar, L. Koenderman, In vivo labeling with $^{2}H_{2}O$ reveals a human neutrophil lifespan of 5.4 days. *Blood* **116**, 625–627 (2010).
14. S. Yona, K. W. Kim, Y. Wolf, A. Mildner, D. Varol, M. Breker, D. Strauss-Ayali, S. Viukov, M. Guilliams, A. Misharin, D. A. Hume, H. Perlman, B. Malissen, E. Zelzer, S. Jung, Fate mapping reveals origins and dynamics of monocytes and tissue macrophages under homeostasis. *Immunity* **38**, 79–91 (2013).
15. A. Viola, F. Munari, R. Sanchez-Rodriguez, T. Scolaro, A. Castegna, The metabolic signature of macrophage responses. *Front. Immunol.* **10**, 1462 (2019).
16. R. Bulla, C. Tripodo, D. Rami, G. S. Ling, C. Agostinis, C. Guarnotta, S. Zorzet, P. Durigutto, M. Botto, F. Tedesco, C1q acts in the tumour microenvironment as a cancer-promoting factor independently of complement activation. *Nat. Commun.* **7**, 10346 (2016).
17. D. Oelschlaegel, T. Weiss Sadan, S. Salpeter, S. Krug, G. Blum, W. Schmitz, A. Schulze, P. Michl, Cathepsin inhibition modulates metabolism and polarization of tumor-associated macrophages. *Cancers* **12**, 2579 (2020).
18. S. Wang, R. Song, Z. Wang, Z. Jing, S. Wang, J. Ma, S100A8/A9 in inflammation. *Front. Immunol.* **9**, 1298 (2018).
19. S. Saeed, J. Quintin, H. H. Kerstens, N. A. Rao, A. Aghajanirefah, F. Matarese, S. C. Cheng, J. Ratter, K. Berentsen, M. A. van der Ent, N. Sharifi, E. M. Janssen-Megens, M. Ter Huurne, A. Mandoli, T. van Schaik, A. Ng, F. Burden, K. Downes, M. Frontini, V. Kumar, E. J. Giamarellos-Bourboulis, W. H. Ouwehand, J. W. van der Meer, L. A. Joosten, C. Wijmenga, J. H. Martens, R. J. Xavier, C. Logie, M. G. Netea, H. G. Stunnenberg, Epigenetic programming of monocyte-to-macrophage differentiation and trained innate immunity. *Science* **345**, 1251086 (2014).
20. R. Y. Ma, A. Black, B. Z. Qian, Macrophage diversity in cancer revisited in the era of single-cell omics. *Trends Immunol.* **43**, 546–563 (2022).
21. L. Fantuzzi, P. Borghi, V. Ciolli, G. Pavlakis, F. Belardelli, S. Gessani, Loss of CCR2 expression and functional response to monocyte chemotactic protein (MCP-1) during the

Downloaded from https://www.science.org at Technische University Eindhoven on October 30, 2026

ERRATUM PUBLISHED 25 SEPTEMBER 2026; SEE LAST PAGE

differentiation of human monocytes: Role of secreted MCP-1 in the regulation of the chemotactic response. *Blood* **94**, 875–883 (1999).
22. M. M. Gubin, E. Esaulova, J. P. Ward, O. N. Malkova, D. Runci, P. Wong, T. Noguchi, C. D. Arthur, W. Meng, E. Alspach, R. F. V. Medrano, C. Fronick, M. Fehlings, E. W. Newell, R. S. Fulton, K. C. F. Sheehan, S. T. Oh, R. D. Schreiber, M. N. Artyomov, High-dimensional analysis delineates myeloid and lymphoid compartment remodeling during successful immune-checkpoint cancer therapy. *Cell* **175**, 1014–1030.e19 (2018).
23. M. R. Horton, J. D. Powell, Quieting T cells with Slfn2. *Nat. Immunol.* **11**, 281–282 (2010).
24. X. Wang, X. Shen, S. Chen, H. Liu, N. Hong, H. Zhong, X. Chen, W. Jin, Reinvestigation of classic T cell subsets and identification of novel cell subpopulations by single-cell RNA sequencing. *J. Immunol.* **208**, 396–406 (2022).
25. H. Spits, D. Artis, M. Colonna, A. Diefenbach, J. P. Di Santo, G. Eberl, S. Koyasu, R. M. Locksley, A. N. McKenzie, R. E. Mebius, F. Powrie, E. Vivier, Innate lymphoid cells — A proposal for uniform nomenclature. *Nat. Rev. Immunol.* **13**, 145–149 (2013).
26. E. Vivier, D. Artis, M. Colonna, A. Diefenbach, J. P. Di Santo, G. Eberl, S. Koyasu, R. M. Locksley, A. N. J. McKenzie, R. E. Mebius, F. Powrie, H. Spits, Innate lymphoid cells: 10 years On. *Cell* **174**, 1054–1066 (2018).
27. N. A. Bezman, C. C. Kim, J. C. Sun, G. Min-Oo, D. W. Hendricks, Y. Kamimura, J. A. Best, A. W. Goldrath, L. L. Lanier, Immunological Genome Project Consortium, Molecular definition of the identity and activation of natural killer cells. *Nat. Immunol.* **13**, 1000–1009 (2012).
28. I. Prager, C. Watzl, Mechanisms of natural killer cell-mediated cellular cytotoxicity. *J. Leukoc. Biol.* **105**, 1319–1329 (2019).
29. M. Efremova, M. Vento-Tormo, S. A. Teichmann, R. Vento-Tormo, CellPhoneDB: Inferring cell-cell communication from combined expression of multi-subunit ligand-receptor complexes. *Nat. Protoc.* **15**, 1484–1506 (2020).
30. M. Cheng, G. Liang, Z. Yin, X. Lin, Q. Sun, Y. Liu, Immunosuppressive role of SPP1-CD44 in the tumor microenvironment of intrahepatic cholangiocarcinoma assessed by single-cell RNA sequencing. *J. Cancer Res. Clin. Oncol.* **149**, 5497–5512 (2023).
31. I. Melero, W. W. Shuford, S. A. Newby, A. Aruffo, J. A. Ledbetter, K. E. Hellstrom, R. S. Mittler, L. Chen, Monoclonal antibodies against the 4-1BB T-cell activation molecule eradicate established tumors. *Nat. Med.* **3**, 682–685 (1997).
32. L. Kalafati, I. Kourtzelis, J. Schulte-Schrepping, X. Li, A. Hatzioannou, T. Grinenko, E. Hagag, A. Sinha, C. Has, S. Dietz, A. M. de Jesus Domingues, M. Nati, S. Sormendi, A. Neuwirth, A. Chatzigeorgiou, A. Ziogas, M. Lesche, A. Dahl, I. Henry, P. Subramanian, B. Wielockx, P. Murray, P. Mirtschink, K. J. Chung, J. L. Schultze, M. G. Netea, G. Hajishengallis, P. Verginis, I. Mitroulis, T. Chavakis, Innate immune training of granulopoiesis promotes anti-tumor activity. *Cell* **183**, 771–785.e12 (2020).
33. R. Romee, M. Rosario, M. M. Berrien-Elliott, J. A. Wagner, B. A. Jewell, T. Schappe, J. W. Leong, S. Abdel-Latif, S. E. Schneider, S. Willey, C. C. Neal, L. Yu, S. T. Oh, Y. S. Lee, A. Mulder, F. Claas, M. A. Cooper, T. A. Fehniger, Cytokine-induced memory-like natural killer cells exhibit enhanced responses against myeloid leukemia. *Sci. Transl. Med.* **8**, 357ra123 (2016).
34. R. J. W. Arts, A. Carvalho, C. La Rocca, C. Palma, F. Rodrigues, R. Silvestre, J. Kleinnijenhuis, E. Lachmandas, L. G. Goncalves, A. Belinha, C. Cunha, M. Oosting, L. A. B. Joosten, G. Matarese, R. van Crevel, M. G. Netea, Immunometabolic pathways in BCG-induced trained immunity. *Cell Rep.* **17**, 2562–2571 (2016).
35. J. Kleinnijenhuis, J. Quintin, F. Preijers, L. A. B. Joosten, C. Jacobs, R. J. Xavier, J. W. van der Meer, R. van Crevel, M. G. Netea, BCG-induced trained immunity in NK cells: Role for non-specific protection to infection. *Clin. Immunol.* **155**, 213–219 (2014).
36. E. Russo, M. Laffranchi, L. Tomaipitinca, A. Del Prete, A. Santoni, S. Sozzani, G. Bernardini, NK cell anti-tumor surveillance in a myeloid cell-shaped environment. *Front. Immunol.* **12**, 787116 (2021).
37. M. A. Cooper, J. M. Elliott, P. A. Keyel, L. Yang, J. A. Carrero, W. M. Yokoyama, Cytokine-induced memory-like natural killer cells. *Proc. Natl. Acad. Sci. U.S.A.* **106**, 1915–1919 (2009).
38. L. Quatrini, F. R. Mariotti, E. Munari, N. Tumino, P. Vacca, L. Moretta, The Immune checkpoint PD-1 in natural killer cells: Expression, function and targeting in tumour immunotherapy. *Cancers* **12**, 3285 (2020).
39. T. Kambayashi, T. M. Laufer, Atypical MHC class II-expressing antigen-presenting cells: Can anything replace a dendritic cell? *Nat. Rev. Immunol.* **14**, 719–730 (2014).
40. N. Nastasi, A. Pasha, G. Bruno, A. Subbiani, L. Pietrovito, A. Leo, L. Scala, L. de Simone, G. Casazza, F. Lunardi, M. L. Taddei, A. Tamburini, A. Tondo, C. Favre, M. Calvani, Blockade of IL-10 signaling ensures mifamurtide efficacy in metastatic osteosarcoma. *Cancers* **15**, 4744 (2023).
41. R. Satija, J. A. Farrell, D. Gennert, A. F. Schier, A. Regev, Spatial reconstruction of single-cell gene expression data. *Nat. Biotechnol.* **33**, 495–502 (2015).
42. G. Yu, L. G. Wang, Y. Han, Q. Y. He, clusterProfiler: An R package for comparing biological themes among gene clusters. *OMICS* **16**, 284–287 (2012).
43. L. Garcia-Alonso, L.-F. Handfield, K. Roberts, K. Nikolakopoulou, R. C. Fernando, L. Gardner, B. Woodhams, A. Arutyunyan, K. Polanski, R. Hoo, C. Sancho-Serra, T. Li, K. Kwakwa, E. Tuck, V. Lorenzi, H. Massalha, M. Prete, V. Kleshchevnikov, A. Tarkowska, T. Porter, C. I. Mazzeo, S. van Dongen, M. Dabrowska, V. Vaskivskyi, K. T. Mahbubani, J.-E. Park, M. Jimenez-Linan, L. Campos, V. Y. Kiselev, C. Lindskog, P. Ayuk, E. Prigmore, M. R. Stratton, K. Saeb-Parsy, A. Moffett, L. Moore, O. A. Bayraktar, S. A. Teichmann, M. Y. Turco, R. Vento-Tormo, Mapping the temporal and spatial dynamics of the human endometrium in vivo and in vitro. *Nat. Genet.* **53**, 1698–1711 (2021).
44. G. Hather, R. Liu, S. Bandi, J. Mettetal, M. Manfredi, W. C. Shyu, J. Donelan, A. Chakravarty, Growth rate analysis and efficient experimental design for tumor xenograft studies. *Cancer Inform.* **13**, 65–72 (2014).

Acknowledgments: We thank the Icahn School of Medicine, the Radboud University Medical Center and the Amsterdam University Medical Center. We would also like to extend the gratitude to the following Mount Sinai core facilities: flow cytometry core, microscopy core, CCMS, and TMII's preclinical imaging core and the animal facility at the Free University Amsterdam. **Funding:** This work was supported by the ERC Advanced Grant TOLERANCE, the NWO Vici grant 91818622, the NIH/NIAID P01 AI168258, the AMC PhD Scholarship, and the ZonMW PTO2 NWS reisbeurs (446001046). **Author contributions:** Conceptualization: W.J.M.M., B.P., A.W.G., and M.G.N. conceptualized and designed experiments. W.J.M.M. supervised the study and held overall responsibility. Supervision: B.P. and J.M. supervised students working on the manuscript. M.M.T.v.L., A.J.P.T., and M.P.J.d.W. supervised their respective research groups. Writing—original draft: B.P. and W.J.M.M. wrote the main manuscript. B.P., L.W., J.M., I.V.M., and R.v.D.M. wrote the Supplementary Materials of the manuscript. Visualization: B.P., S.R.J.H., T.A., Y.v.E., L.W., W.W., J.M., and I.V.M., produced figures. W.J.M.M. supervised the overall figure production. Investigation: W.W., A.R., J.M., G.P., G.A.O.C., and J.H.C.M.K. produced HDL-MTP. B.P., M.M.T.v.L., S.R.J.H., T.A., Y.v.E., J.D., D.P.S., J.M., D.H., Y.C.T., E.K., C.P.-M., T.J.B., R.v.d.M., R.D., Z.A.F., and A.W.G. coordinated and performed in vivo and ex vivo mouse studies. Flow cytometry was performed by B.P., M.M.T.v.L., S.R.J.H., T.A., Y.v.E., J.D., I.S., T.P., and J.O. scRNA-seq was performed and analyzed by B.P., L.W., T.A., and J.D. Cytokine analysis was performed and analyzed by B.P. and L.W. Formal analysis: W.W., A.R., J.M., G.P., G.A.O.C., and J.H.C.M.K. analyzed HDL-MTP. B.P., S.R.J.H., T.A., Y.v.E., J.D., D.P.S., J.M., D.H., Y.C.T., E.K., C.P.-M., T.J.B., and R.v.d.M. analyzed in vivo and ex vivo mouse studies. Flow cytometry was analyzed by B.P., M.M.T.v.L., S.R.J.H., T.A., Y.v.E., J.D., I.S., T.P., and J.O. scRNA-seq was analyzed by B.P., L.W., I.V.M., S.R.J.H., T.A., Y.v.E., J.D., M.P.J.d.W., Y.Z., and C.G. Cytokine analysis was analyzed by L.W. Project administration: L.W., B.P., J.M., W.J.M.M., and D.S. Validation: L.W., B.P., J.M., and D.S. Methodology: L.W., A.J.P.T., B.P., G.P., J.M., M.M.T.v.L., C.P.-M., M.P.J.d.W., R.D., and W.J.M.M. contributed to the methodology. Funding acquisition: B.P., Z.A.F., M.G.N., M.P.J.d.W., A.W.G., and W.J.M.M. Writing—review and editing: All authors contributed to review and editing of the manuscript. **Competing interests:** W.J.M.M., L.A.B.J., J.O., Z.A.F., and M.G.N. are scientific cofounders of and have equity in Trained Therapeutix Discovery. W.J.M.M. and Z.A.F. have consulting agreements with Trained Therapeutix Discovery. W.J.M.M. is the shareholder and CSO of Trained Therapeutix Discovery and founder, shareholder, and CTO of BioTrip. J.H.C.M.K., G.A.O.C., B.P., and T.J.B. have positions at Trained Therapeutix Discovery. All other authors declare that they have no competing interests. **Data and materials availability:** All data and code needed to evaluate and reproduce the results in the paper are present in the paper and/or the Supplementary Materials. Sequencing data are deposited in the Gene Expression Omnibus (GEO) under the accession ID: GSE235598. Further information and requests for resources and reagents should be directed to and will be W.J.M.M. (willem.mulder@radboudumc.nl).

Submitted 21 October 2024
Accepted 25 November 2025
Published 1 January 2026
10.1126/sciadv.adu0292

Downloaded from https://www.science.org at Technische University Eindhoven on October 30, 2026

Erratum

Post date 25 September 2026

Erratum for the Research Article "Systemically inducing trained immunity overcomes solid tumors' immunosuppressive microenvironment" by B. Priem *et al.*

The original version of the Research Article, "Systemically inducing trained immunity overcomes solid tumors' immunosuppressive microenvironment" by B. Priem *et al.*, did not include animal use or ethics approval information. This information was included in their original manuscript but was inadvertently removed during the revision process.

The following corrections have been implemented:

- The sections "Inbred mice strains," "Tumor inoculation and treatment regimen," and "Cell lines (B16F10, 4T1, LLC and PANC-02)," which include animal use and ethics approval information, were added to the Materials and Methods.

The authors' conclusions are not affected by these corrections. The PDF and online version have been updated.

Downloaded from https://www.science.org at Technische University Eindhoven on October 30, 2026

10.1126/sciadv.aem0051

ScienceAdvances

Systemically inducing trained immunity overcomes solid tumors' immunosuppressive microenvironment

Bram Priem, Lisa Willemsen, Tom Anbergen, Yuri van Elsas, Jeroen Deckers, David P. Schrijver, Stijn R.J. Hofstraat, Iris V. Messing, Jazz Munitz, Dionne Honing, Geoffrey Prévot, Yohana C. Toner, Judit Morla, William Wang, Anna Ranzenigo, Isabella Sirchia, Tomas Post, Raphaël Duivenvoorden, Ewelina Kluza, Glenn A.O. Cremers, Joost H.C.M Kreijtz, Carlos Pérez-Medina, Mandy M.T. van Leent, Abraham J.P. Teunissen, Roy van der Meel, Yi Zhou, Chris Glass, Jordi Ochando, Leo A.B. Joosten, Zahi A. Fayad, Romana T. Netea-Maier, Mihai G. Netea, Menno P.J. de Winther, Thijs J. Beldman, Arjan W. Griffioen, and Willem J.M. Mulder

Sci. Adv. **12** (1), eadu0292. DOI: 10.1126/sciadv.adu0292

View the article online
https://www.science.org/doi/10.1126/sciadv.adu0292
Permissions
https://www.science.org/help/reprints-and-permissions

Downloaded from https://www.science.org at Technische University Eindhoven on October 30, 2026

Use of this article is subject to the Terms of service

Science Advances (ISSN 2375-2548) is published by the American Association for the Advancement of Science. 1200 New York Avenue NW, Washington, DC 20005. The title *Science Advances* is a registered trademark of AAAS.

Copyright © 2026 The Authors, some rights reserved; exclusive licensee American Association for the Advancement of Science. No claim to original U.S. Government Works. Distributed under a Creative Commons Attribution NonCommercial License 4.0 (CC BY-NC).